International Journal of Solids and Structures xxx (2015) xxx–xxx

Contents lists available at ScienceDirect

International Journal of Solids and Structures

journal homepage: www.elsevier.com/locate/ijsolstr

Homogenization of linear elastic properties of short-fiber reinforced composites – A comparison of mean field and voxel-based methods

Viktor Müller [a,*], Matthias Kabel [b], Heiko Andrä [b], Thomas Böhlke [a]

[a] Chair for Continuum Mechanics, Institute of Engineering Mechanics, Karlsruhe Institute of Technology (KIT), Germany
[b] Flow and Material Simulation, Fraunhofer ITWM, Germany

ARTICLE INFO

Article history:
Received 7 April 2014
Received in revised form 3 December 2014
Available online xxxx

Keywords:
Mean field homogenization
Full field simulation
Self-consistent method
Interaction direct derivative
Fast Fourier transformation
Short-fiber reinforced composites

ABSTRACT

The main contribution of this work lies in the detailed comparison of the predictions of linear elastic properties of mean field homogenization approaches and full field, voxel-based homogenization methods for short-fiber reinforced materials. In the former case, the self-consistent, the interaction direct derivative and a two-step-bounding approach, applying the Hashin–Shtrikman bounds, are used. In the latter case, the boundary value problem for representative volume elements is solved using fast Fourier transformation. Model microstructures with unidirectional aligned and two misaligned fiber configurations are considered exemplarily. Fiber volume fractions of 13%, 17% and 21% and phase contrasts of 44, 100 and 1000 in the elastic moduli have been taken into account. The different homogenization schemes are compared by means of effective directional dependent Young's modulus. This detailed comparison shows that mean field and full field solutions deliver similar results for moderate phase contrasts and volume fractions. Especially in the range of realistic phase contrasts like 44 for a composite of polypropylene and glass, the mean field approaches pose reliable alternatives for full field solution. Large phase contrasts result in relative deviations of up to 68%.

© 2015 Elsevier Ltd. All rights reserved.

1. Introduction

Since the mechanical behavior of fiber reinforced lightweight materials is crucially dominated by their microstructure, a reliable dimensioning has to take into consideration the properties of this microstructure. Especially, the microstructure of injection-molded thin parts manufactured of short-fiber reinforced composites exhibit a layer-wise setup (Bernasconi et al., 2008, 2012). While in the boundary layers, the majority of the fibers is oriented in the main flow direction of the material during manufacturing, in the core layer, the fibers are predominantly oriented perpendicular to the main flow direction. Experimentally, the microstructure properties can be examined, e.g., through micro-computer tomography measurements (Maire and Withers, 2013; Bernasconi et al., 2012; Shen et al., 2004).

In order to calculate the effective material behavior based on microstructure data, several methods of homogenization have been suggested in literature (Kanouté et al., 2009; Geers et al., 2010). Among them, two basic groups can be identified: Mean field and full field approaches. Within the first group, bounding and estimating mean field methods can be distinguished. Bounding methods specify an admissible range of possible effective properties for given microstructural information. The size of this range depends on microstructural properties like the volume fraction, material properties of the phases and, additionally on the specific assumptions made for the homogenization approach. Exemplarily, within the first order or simple bounds, known as the Voigt and Reuss bounds (Voigt, 1889; Reuss, 1929), the strain field or the stress field, respectively, is assumed to be uniform throughout the heterogeneous material. In both approaches the only microstructural information taken into account are the volume fractions. Simple bounds enclose a wide range of admissible effective properties. Tighter bounds have been provided by Hashin and Shtrikman (1962a,b, 1963) and extended by Willis (1977) and Böhlke and Lobos (2014) for anisotropic materials. Based on a variational principle and a comparison material, this approach has been applied to nonlinear composites (Talbot and Willis, 1992; Willis, 1986) and also to power-law composites (Suquet, 1993), to mention only few. In contrary to the bounding approaches, estimating methods approximate effective properties. The Mori–Tanaka (Mori and Tanaka, 1973), the generalized self-

* Corresponding author.
E-mail addresses: viktor.mueller@kit.edu (V. Müller), matthias.kabel@itwm.fraunhofer.de (M. Kabel), heiko.andrae@itwm.fraunhofer.de (H. Andrä), thomas.boehlke@kit.edu (T. Böhlke).

http://dx.doi.org/10.1016/j.ijsolstr.2015.02.030
0020-7683/© 2015 Elsevier Ltd. All rights reserved.

Please cite this article in press as: Müller, V., et al. Homogenization of linear elastic properties of short-fiber reinforced composites – A comparison of mean field and voxel-based methods. Int. J. Solids Struct. (2015), http://dx.doi.org/10.1016/j.ijsolstr.2015.02.030

consistent (SC) (Christensen and Lo, 1979) and the interaction direct derivative (IDD) (Zheng and Du, 2001) estimates are prominent representatives of such mean field schemes, which take the interaction of the inclusions into account. Originally developed to approximate the effective behavior of a polycrystalline structure based only on the properties of a single crystal (Kröner, 1977), the SC method has been applied to granular and also particulate systems (Willis, 1981). Based on the Eshelby solution (Eshelby, 1957), the general idea is, that each inclusion is embedded in an infinite matrix, which possesses the properties of the effective material. Due to this choice of the matrix material, the SC method has an inherently implicit character. Hill (1965) and Budiansky (1965) extended the SC method to multi-phase materials. The major shortcoming of SC is, that the interaction between the inclusions and the surrounding matrix is not considered directly. This drawback is the main motivation to apply methods like IDD, which are based on the three-phase model. Here, one inclusion interacts with the matrix directly and with the other inclusions through the effective medium. Another mean field approach is based on two-step methods (TS) (Pierard et al., 2004; Doghri and Tinel, 2006). This method can be applied to homogenize multi-phase particulate composites. The phases, which can be also fibers, are distinguished by their geometrical shape, their orientation and material properties. The first step within this method consists of the decomposition of the microstructure in as many domains as there exist different inclusions. In a first step, each domain is quasi-homogenized individually, and then, in a second step, all domains are homogenized to determine the effective properties. These methods have been applied to thermo-elastic (Pierard et al., 2004) and elasto-plastic materials (Doghri and Friebel, 2005). The main motivation for the introduction of the TS method is that this method can be applied to a much larger class of microstructures compared to second-order bounding schemes. A comparison of the SC method, the IDD approach and the TS scheme with experimental data is given in Müller et al. (2015).

In the last years, numerical homogenization techniques based on full field simulations have made significant progress (Suquet, 1987; Guedes and Kikuchi, 1990; Ghosh et al., 1995; Moulinec and Suquet, 1994; Andrä et al., 2013b). For full field methods, the microstructure is represented by a representative volume element (RVE), which is subjected to a macroscopic load. After determining the local fields in the RVE caused by external load (e.g., by FEM, BEM, FFT), the effective response of the RVE can be calculated by volume averaging of the full field solution. This approach allows for the treatment of complicated microstructures and is also applicable for inelastic material laws, e.g., plasticity or viscoplasticity. Generally, the choice of the RVE size and the implementation of proper boundary conditions with regard on the considered microstructure are issues to be solved when applying this method (Dirrenberger et al., 2014).

In this paper, the Fourier method has been chosen for the calculation of the full field solutions. The Fourier method was first proposed by Moulinec and Suquet (1994). This method applies the fast Fourier transformation (FFT) to solve integral equations of Lippmann–Schwinger type (Zeller, 1973; Kröner, 1977), which are equivalent to the local periodic cell problems in numerical homogenization. Since no meshing is required and the assembly of the linear system is avoided, the memory needed for solving the problem is significantly reduced compared to other methods. Primarily due to the striking speed of available FFT implementations (Frigo and Johnson, 1998, 2005; Johnson and Frigo, 2007), this approach has become popular in recent years, in particular for real world industrial applications (Andrä et al., 2013a). A full field FFT approach has been compared to various mean field methods based on artificial variation of the properties of the constituents of a composite consisting of a matrix and spherical inclusions (Ghossein and Lévesque, 2012) and to experimental data (Spahn et al., 2014).

The outline of the present paper is as follows: In Section 2, the theoretical background of the applied SC scheme, the IDD approach, the TS method and the FFT full field method is given. The generated model microstructures and their properties are described in Section 3. Here, besides a microstructure with unidirectional aligned fibers, two microstructure with unaligned fiber configurations inspired by the characteristics of the microstructure of short-fiber reinforced composites are considered. In Section 4, the numerical results of the mean field methods are compared to the full field solutions for all microstructure types. A summary and conclusions are given in Section 5.

Notation. A direct tensor notation is preferred throughout the text, see, e.g., (Truesdell and Noll, Jan. 2004; Šilhavý, 1997). If tensor components are used, then Latin indices are used and the Einstein's summation convention is applied. Vectors and second-order tensors are denoted by lowercase and uppercase bold letters, e.g., $\boldsymbol{a}$ and $\boldsymbol{A}$, respectively. The composition of two second-order or two fourth-order tensors is formulated by $\boldsymbol{AB}$ and $\mathbb{AB}$. A linear mapping of second-order tensors by a fourth-order tensor is written as $\boldsymbol{A} = \mathbb{C}[\boldsymbol{B}]$. The inner product between second-order tensors is denoted by $\boldsymbol{A} \cdot \boldsymbol{B}$. We define the operator $\square$ via $(\boldsymbol{A}\square\boldsymbol{B})[\boldsymbol{C}] = \boldsymbol{ACB}$, the dyadic product $\otimes$ by $(\boldsymbol{A} \otimes \boldsymbol{B})[\boldsymbol{C}] = (\boldsymbol{B} \cdot \boldsymbol{C})\boldsymbol{A}$ and the operator $[\![\cdot]\!]$ by $(\boldsymbol{a} \otimes \boldsymbol{b}) \cdot (\mathbb{C}[\![\boldsymbol{a} \otimes \boldsymbol{b}]\!]) = (\boldsymbol{a} \otimes \boldsymbol{a}) \cdot (\mathbb{C}[\boldsymbol{b} \otimes \boldsymbol{b}])$. Arbitrary vectors $\boldsymbol{a}$ and $\boldsymbol{b}$, second-order tensors $\boldsymbol{A}, \boldsymbol{B}$ and $\boldsymbol{C}$ and a fourth-order tensor $\mathbb{C}$ are used in the foregoing definitions. The identity on symmetric second-order tensors is denoted by $\mathbb{I}^s$. The brackets $\langle\cdot\rangle$, e.g., $\langle\varepsilon\rangle$, indicate ensemble averaging which for ergodic media can be identified with volume averages in the infinite volume limit. A superimposed bar, e.g., $\bar{\varepsilon}$, indicates that the quantity refers to the macroscale. The discrete fast Fourier transformation operation is denoted by DFT. Quantities in Fourier space are indicated by $\hat{(\cdot)}$.

Abbreviations. To distinguish the regarded methods and the considered microstructure types, several abbreviations have to be introduced as a reference for the reader in Table 1.

2. Determination of elastic properties

2.1. Modeling preliminaries

In the present work, short-fiber reinforced composites (SFRC) are considered, where the matrix and the arbitrary oriented fibers are assumed to be linear isotropic with piecewise constant properties. The microstructure $\Omega = \Omega_F \cup \Omega_M$ consists of a matrix Ω_M and a set of N fibers $\Omega_F = \{\Omega_\alpha : \alpha = 1, \ldots, N\}$. The matrix is characterized by its stiffness tensor $\mathbb{C}_M$ and volume fraction c_M. Accordingly, the fiber with number α is specified by the orientation of the axis $\boldsymbol{n}_\alpha$, the length l_α, the radius r_α, the volume fraction c_α and the stiffness

Table 1
Abbreviations used in the present paper due to convenient handling.

BS	Basic scheme of the FFT solution
DFT	DFT discrete fast Fourier transformation
FFT	Fast Fourier transformation
HS	Hashin–Shtrikman
HS−	Hashin–Shtrikman lower bound
HS+	Hashin–Shtrikman upper bound
IDD	Interaction direct derivative
MF	Mean field
RVE	Representative volume element
SC	Self-consistent
SFRC	Short-fiber reinforced composite
TS	Two step (mean field approach)
TP	Thin plate (microstructure type)
UD	Unidirectional (microstructure type)

Please cite this article in press as: Müller, V., et al. Homogenization of linear elastic properties of short-fiber reinforced composites – A comparison of mean field and voxel-based methods. Int. J. Solids Struct. (2015), http://dx.doi.org/10.1016/j.ijsolstr.2015.02.030

tensor $\mathbb{C}_\alpha$. The aspect ratio $a_\alpha = l_\alpha/(2r_\alpha)$ denotes the ratio of the length to the diameter of each fiber. The total fiber volume fraction is indicated with $c_F = 1 - c_M = \sum_{\alpha=1}^{N} c_\alpha$. The material behavior of the fibers is assumed to be uniform, e.g., $\mathbb{C}_\alpha = \mathbb{C}_F$ for $\alpha = 1, \ldots, N$.

2.2. Mean field homogenization

2.2.1. Self-consistent homogenization

The effective elastic stiffness tensor $\bar{\mathbb{C}}$ can be formulated as ensemble average using the strain localization tensor $\mathbb{A}$ (Kröner, 1977). In case of ergodic media, the ensemble average can be interpreted as a volume average. For microstructures with piecewise constant properties, the effective elastic stiffness is then given by

$$\bar{\mathbb{C}} = \mathbb{C}_M + \sum_{\alpha=1}^{N} c_\alpha (\mathbb{C}_\alpha - \mathbb{C}_M)\mathbb{A}_\alpha, \tag{1}$$

where $\mathbb{A}_\alpha$ describes the average strain localization tensor in terms of phase α or fiber α, respectively. For the formulation of the effective stiffness in Eq. (1), the normalization condition $\langle \mathbb{A} \rangle = \mathbb{I}^s$ has been used. The SC homogenization scheme generally assumes that each fiber is embedded in an infinite homogeneous matrix with the properties of the effective material $\bar{\mathbb{C}} = \mathbb{C}^{SC}$. The inclusion problem is solved based on the single inclusion formula of Eshelby (1957). Thus, for the special case of an ellipsoidal approximation of the cylindrical fibers, the strain localization $\mathbb{A}_\alpha$ is a function of the effective stiffness $\mathbb{C}^{SC}$, the stiffness $\mathbb{C}_\alpha$ and the geometry of the ellipsoid $\boldsymbol{Z}_\alpha$, which contains the information about the fiber axis orientation:

$$\mathbb{A}_\alpha = \mathbb{A}(\mathbb{C}^{SC}, \mathbb{C}_\alpha, \boldsymbol{Z}_\alpha) = \left(\mathbb{I}^s + \mathbb{P}_\alpha^{SC}\left(\mathbb{C}_\alpha - \mathbb{C}^{SC}\right)\right)^{-1}. \tag{2}$$

Herein, $\mathbb{P}_\alpha^{SC}$ denotes Hill's polarization tensor (see equation 4.34 in Willis, 1981):

$$\mathbb{P}_\alpha^{SC}(\mathbb{C}^{SC}, \boldsymbol{Z}_\alpha) = \frac{1}{4\pi \det(\boldsymbol{Z}_\alpha)} \int_S \mathbb{H}(\mathbb{C}^{SC}, \boldsymbol{n}) \left(\boldsymbol{n} \cdot \left(\boldsymbol{Z}_\alpha^{-\mathsf{T}} \boldsymbol{Z}_\alpha^{-1} \boldsymbol{n}\right)\right)^{-3/2} \mathrm{d}S, \tag{3}$$

with $\mathbb{H}(\mathbb{C}^{SC}, \boldsymbol{n}) = \mathbb{I}^s(\boldsymbol{K}^{-1}\square(\boldsymbol{n}\otimes\boldsymbol{n}))\mathbb{I}^s$ and $\boldsymbol{K} = \mathbb{C}^{SC}[\![\boldsymbol{n}\otimes\boldsymbol{n}]\!]$. The polarization tensor $\mathbb{P}_\alpha^{SC}$ depends on the stiffness $\mathbb{C}^{SC}$ and the ellipsoidal geometry of the fibers $\boldsymbol{Z}_\alpha$:

$$\|\boldsymbol{Z}_\alpha \boldsymbol{x}\|^2 = \boldsymbol{x} \cdot \left(\boldsymbol{Z}_\alpha^{\mathsf{T}} \boldsymbol{Z}_\alpha \boldsymbol{x}\right) \leqslant 1. \tag{4}$$

$\boldsymbol{x}$ denotes a position vector in the three-dimensional space. The inverse eigenvalues of $\boldsymbol{Z}_\alpha$ correspond to the half axis of the ellipsoid with the number α. In Eq. (3), $\mathrm{d}S$ is a surface element of the unit sphere $S := \{\boldsymbol{n} \in \mathbb{R}^3 : \|\boldsymbol{n}\| = 1\}$, and $\det(\boldsymbol{Z}_\alpha)$ represents the determinant of $\boldsymbol{Z}_\alpha$.

The stiffness $\mathbb{C}^{SC}$ can be computed by solving the following implicit equation resulting from Eqs. (1) and (2) and the SC approximation $\bar{\mathbb{C}} = \mathbb{C}^{SC}$ (Willis, 1986):

$$\mathbb{C}^{SC} = \mathbb{C}_M + \sum_{\alpha=1}^{N} c_\alpha (\mathbb{C}_\alpha - \mathbb{C}_M)\left(\mathbb{I}^s + \mathbb{P}_\alpha^{SC}\left(\mathbb{C}_\alpha - \mathbb{C}^{SC}\right)\right)^{-1}. \tag{5}$$

This equation for the unknown tensorial quantity $\mathbb{C}^{SC}$ is solved numerically using a Newton–Raphson algorithm combined with a line search procedure. To determine Hill's polarization tensor $\mathbb{P}_\alpha^{SC}$ numerically, a Gaussian quadrature over the unit sphere according to Mura (1987) is used.

2.2.2. Interaction direct derivative

The interaction direct derivative (IDD) estimate, proposed by Zheng and Du (2001) is based on the generalized self-consistent scheme (GSCS) (Christensen and Lo, 1979), which for its part is based on the three-phase model. In the three-phase model, the inclusions are embedded in a finite matrix material region. This inclusion-matrix cell itself is embedded in the unbounded linear elastic medium with the effective properties. The difference between the three-phase model and the IDD estimate can be identified in the determination of the stresses in the inclusions: In contrary to the three-phase model, Zheng and Du (2001) assume an unbounded medium with the properties of the matrix for the embedding of the inclusion in the matrix material. Du and Zheng (2002) have proven that the stresses in the inclusions are approximated by this assumption with an error of second order of the inclusion volume fraction. The advantage of the IDD is its explicit structure, which is valid for multi-phase composites with different material symmetries and inclusion distributions.

The following equation gives the IDD estimation of the properties of the effective medium:

$$\mathbb{C}^{IDD} = \mathbb{C}_M + \left(\mathbb{I}^s - \sum_{\beta=1}^{N} c_\beta (\mathbb{C}_\beta - \mathbb{C}_M)\mathbb{N}_\beta \mathbb{P}_\beta^D\right)^{-1} \sum_{\alpha=1}^{N} c_\alpha (\mathbb{C}_\alpha - \mathbb{C}_M)\mathbb{N}_\alpha, \tag{6}$$

with $\mathbb{N}_\alpha = \left(\mathbb{I}^s + \mathbb{P}_\alpha(\mathbb{C}_\alpha - \mathbb{C}_M)\right)^{-1}$. Here, $\mathbb{P}_\alpha = \mathbb{P}(\mathbb{C}_M, \boldsymbol{Z}_\alpha)$ is Hill's polarization tensor as defined in Eq. (3) (with $\mathbb{C}^{SC}$ replaced by $\mathbb{C}_M$). If the matrix-inclusion cell has an ellipsoidal shape, then, $\mathbb{P}_\alpha^D = \mathbb{P}(\mathbb{C}_M, \boldsymbol{Z}_\alpha^D)$ is the polarization tensor corresponding to an ellipsoidal inclusion with geometry of the matrix-inclusion cell $\boldsymbol{Z}_\alpha^D$, which is embedded in an infinite matrix with the stiffness $\mathbb{C}_M$. The shape of the matrix-inclusion cell defines the inclusion distribution in the composite (Zheng and Du, 2001). In the present work, this shape is assumed to be equal to the shape of the spheroidal approximation $\boldsymbol{Z}_\alpha$ of the corresponding inclusion itself.

Particularly if the distribution is equal for all inclusions ($\boldsymbol{Z}_\alpha^D = \boldsymbol{Z}^D$), the IDD estimate is equivalent to the Hashin–Shtrikman estimate of Ponte Castañeda and Willis (1995), which is based on the Hashin–Shtrikman variational structure in the form developed by Willis (1977, 1978). A detailed discussion of the relation of IDD to the estimate of Ponte Castañeda and Willis (1995) and, e.g., Mori–Tanaka can be found in Zheng and Du (2001) and Du and Zheng (2002).

2.2.3. A two-step bounding method

The SC and the IDD approaches lead to estimates of the effective elastic moduli. The two-step (TS) method provides an admissible range for the effective elastic properties. It should be noted, however, that the TS homogenization applying the HS method based on constant stress polarization and two subsequent steps does not represent a rigorous second-order bounding scheme.

The first step of the TS approach consists of a decomposition of the microstructure into as many domains as there are different fibers (Pierard et al., 2004). Thus, fibers of the same shape and orientation are aggregated into unidirectional domains. The fiber volume fraction in the domains corresponds to the total fiber volume fraction c_F. For each of these domains, the upper and lower bounds, denoted by $\mathbb{C}_\alpha^{UD+}$ and $\mathbb{C}_\alpha^{UD-}$, respectively, are calculated using the unidirectional (UD) special case of the second-order HS bounds. Assuming the fiber material being stiffer than the matrix material leads to the following prescriptions for $\mathbb{C}_\alpha^{UD+}$ and $\mathbb{C}_\alpha^{UD-}$ (Willis, 1977):

$$\begin{aligned} \mathbb{C}_\alpha^{UD+} &= \mathbb{C}_\alpha + (1 - c_F)(\mathbb{C}_M - \mathbb{C}_\alpha)\left(\mathbb{I}^s + c_F \mathbb{P}_\alpha^{UD}(\mathbb{C}_M - \mathbb{C}_\alpha)\right)^{-1}, \\ \mathbb{C}_\alpha^{UD-} &= \mathbb{C}_M + c_F(\mathbb{C}_\alpha - \mathbb{C}_M)\left(\mathbb{I}^s + (1 - c_F)\mathbb{P}_\alpha^{UD}(\mathbb{C}_\alpha - \mathbb{C}_M)\right)^{-1}. \end{aligned} \tag{7}$$

Hill's polarization tensor $\mathbb{P}_\alpha^{UD}$ is known explicitly for the case of unidirectionally aligned ellipsoidal inclusions. The resulting bounds exhibit a transversely isotropic linear elastic behavior. If each fiber

Please cite this article in press as: Müller, V., et al. Homogenization of linear elastic properties of short-fiber reinforced composites – A comparison of mean field and voxel-based methods. Int. J. Solids Struct. (2015), http://dx.doi.org/10.1016/j.ijsolstr.2015.02.030

is unique in terms of direction, geometry or material properties, then N domains have to be considered. In Eq. (7), α depicts the number of the particular domain with $\alpha \in \{1,\dots,N\}$.

In the second step, all domains are homogenized like a granular structure, again using the HS bounds. Herein, only corresponding bounds are combined: the lower (upper) bound of the domains is homogenized with the lower (upper) bound for the granular structure. The resulting stiffness tensors are denoted by $\mathbb{C}^{\mathrm{TS}-}$ and $\mathbb{C}^{\mathrm{TS}+}$, respectively:

$$\mathbb{C}^{\mathrm{TS}\pm} = \sum_{\alpha=1}^{N} \frac{c_\alpha}{c_\mathrm{F}} \mathbb{C}_\alpha^{\mathrm{UD}\pm} \mathbb{A}_\alpha^{\pm} = \sum_{\alpha=1}^{N} \frac{c_\alpha}{c_\mathrm{F}} \mathbb{C}_\alpha^{\mathrm{UD}\pm} \mathbb{M}_\alpha^{\pm} \langle \mathbb{M}^{\pm} \rangle^{-1}, \tag{8}$$

with

$$\mathbb{M}_\alpha^{\pm} = \left(\mathbb{I}^{\mathrm{s}} + \mathbb{P}_0 \left(\mathbb{C}_\alpha^{\mathrm{UD}\pm} - \mathbb{C}_0^{\pm}\right)\right)^{-1}, \langle \mathbb{M}^{\pm} \rangle = \sum_{\beta=1}^{N} \frac{c_\beta}{c_\mathrm{F}} \left(\mathbb{I}^{\mathrm{s}} + \mathbb{P}_0 \left(\mathbb{C}_\beta^{\mathrm{UD}\pm} - \mathbb{C}_0^{\pm}\right)\right)^{-1}. \tag{9}$$

Here, $\mathbb{P}_0$ is Hill's polarization tensor for a spherical inclusion embedded in a matrix with the comparison stiffness $\mathbb{C}_0^{\pm}$. In case of the lower (upper) HS bound, for this comparison material, the minimum (maximum) isotropic part of all domain stiffnesses $\mathbb{C}_\alpha^{\mathrm{UD}-}$ ($\mathbb{C}_\alpha^{\mathrm{UD}+}$) is taken.

2.3. Full field homogenization

2.3.1. Periodic boundary value problem

For the homogenization of a heterogeneous, periodic medium with local stiffness $\mathbb{C}(\boldsymbol{x})$, a periodic boundary value problem (BVP) for the displacement fluctuations $\tilde{\boldsymbol{u}}$ on a rectangular cuboid Ω, which is often called unit-cell, statistic or representative volume element (RVE), has to be solved:

$$\begin{cases} \operatorname{div}(\boldsymbol{\sigma}(\boldsymbol{x})) = \boldsymbol{0}, & \boldsymbol{x} \in \Omega, \\ \boldsymbol{\sigma}(\boldsymbol{x}) = \mathbb{C}(\boldsymbol{x})[\boldsymbol{\varepsilon}(\boldsymbol{x})], & \boldsymbol{x} \in \Omega, \\ \boldsymbol{\varepsilon}(\boldsymbol{x}) = \bar{\boldsymbol{\varepsilon}} + \operatorname{sym}(\operatorname{grad}(\tilde{\boldsymbol{u}}(\boldsymbol{x}))) & \boldsymbol{x} \in \Omega, \\ \tilde{\boldsymbol{u}}(\boldsymbol{x}) \quad \text{periodic}, & \boldsymbol{x} \in \partial\Omega, \\ (\boldsymbol{\sigma}\boldsymbol{n})(\boldsymbol{x}) \quad \text{anti-periodic}, & \boldsymbol{x} \in \partial\Omega. \end{cases} \tag{10}$$

For all constant strains $\bar{\varepsilon}$, the problem (10) is uniquely solvable in the space

$$\left\{ \tilde{\boldsymbol{u}} \in \left(H^{1,\#}(\Omega)\right)^3 : \langle \tilde{\boldsymbol{u}} \rangle_\Omega := \int_\Omega \tilde{\boldsymbol{u}}(x)\, \mathrm{d}\Omega = \boldsymbol{0} \right\}, \tag{11}$$

with $H^{1,\#}(\Omega)$ being the closure of $C^{\infty,\#}(\Omega) = \{\boldsymbol{v} \in C^{\infty}(\Omega) : \boldsymbol{v}$ periodic$\}$ in $H^1(\Omega)$ (see, e.g., Bakhvalov and Panasenko, 1989; Cioranescu and Donato, 1999). In the rectangular cuboid, the considered microstructure is represented in a binary manner using a regular three-dimensional voxel discretization.

2.3.2. Equivalent strain and stress based Lippmann–Schwinger equation

By introducing a homogeneous comparison material of stiffness $\mathbb{C}_0$ and the stress polarization

$$\boldsymbol{p}(\boldsymbol{x}) = (\mathbb{C}(\boldsymbol{x}) - \mathbb{C}_0)[\boldsymbol{\varepsilon}(\boldsymbol{x})], \tag{12}$$

the constitutive equation for the stress $\boldsymbol{\sigma}(\boldsymbol{x}) = \mathbb{C}(\boldsymbol{x})[\boldsymbol{\varepsilon}(\boldsymbol{x})]$ can be transformed as follows

$$\boldsymbol{\sigma}(\boldsymbol{x}) = \mathbb{C}_0[\boldsymbol{\varepsilon}(\boldsymbol{x})] + \boldsymbol{p}(\boldsymbol{x}). \tag{13}$$

For known stress polarization $\boldsymbol{p}(\boldsymbol{x})$ with support in Ω, e.g., $\operatorname{supp}(\boldsymbol{p}) \subseteq \Omega$, the solution of $\operatorname{div}(\boldsymbol{\sigma}(\boldsymbol{x})) = \boldsymbol{0}$ can be expressed by using the nonlocal elastic Green operator $\mathbb{G}_0$ for strains associated with the comparison material $\mathbb{C}_0$ (Kröner, 1977)

$$\boldsymbol{\varepsilon}(\boldsymbol{x}) = \bar{\boldsymbol{\varepsilon}} - (\mathbb{G}_0 * \boldsymbol{p})(\boldsymbol{x}), \tag{14}$$

where the convolution is defined by

$$(\mathbb{G}_0 * \boldsymbol{p})(\boldsymbol{x}) = \int_\Omega \mathbb{G}_0(\boldsymbol{x} - \boldsymbol{y})[\boldsymbol{p}(\boldsymbol{y})]\, \mathrm{d}\Omega. \tag{15}$$

Inserting (12) into (14), the strain based formulation of the Lippmann–Schwinger equation is derived:

$$(\mathbb{I}^{\mathrm{s}} + \mathbb{B}_\varepsilon)[\boldsymbol{\varepsilon}(\boldsymbol{x})] := \boldsymbol{\varepsilon}(\boldsymbol{x}) + (\mathbb{G}_0 * ((\mathbb{C} - \mathbb{C}_0)[\boldsymbol{\varepsilon}(\boldsymbol{x})]))(\boldsymbol{x}) = \bar{\boldsymbol{\varepsilon}}. \tag{16}$$

This integral equation is equivalent to an integral equation for the stress (Kröner, 1971)

$$(\mathbb{I}^{\mathrm{s}} + \mathbb{B}_{\boldsymbol{\sigma}})[\boldsymbol{\sigma}(\boldsymbol{x})] := \boldsymbol{\sigma}(\boldsymbol{x}) + (\mathbb{L}_0 * ((\mathbb{S} - \mathbb{S}_0)[\boldsymbol{\sigma}(\boldsymbol{x})]))(\boldsymbol{x}) = \bar{\boldsymbol{\sigma}}, \tag{17}$$

with the local compliance $\mathbb{S}(\boldsymbol{x}) = \mathbb{C}^{-1}(\boldsymbol{x})$, the compliance of the comparison material $\mathbb{S}_0 = \mathbb{C}_0^{-1}$ and the macroscopic stress $\bar{\boldsymbol{\sigma}} = \mathbb{C}_0[\bar{\boldsymbol{\varepsilon}}]$. The Green operator $\mathbb{L}_0$ for stresses associated with the comparison material $\mathbb{C}_0$ can be determined from the Green operator $\mathbb{G}_0$ for strains by

$$\mathbb{L}_0 = \mathbb{C}_0 - \mathbb{C}_0 \mathbb{G}_0 \mathbb{C}_0. \tag{18}$$

For the sake of a simpler notation, the dependency of the quantities on the spatial position $\boldsymbol{x}$ is not noted in the following equations anymore.

2.3.3. Energy and strain equivalence principle

With the use of the energy equivalence principle (Hill condition)

$$\frac{1}{2}\langle \boldsymbol{\varepsilon}_\alpha \cdot \mathbb{C}[\boldsymbol{\varepsilon}_\beta] \rangle = \frac{1}{2}\langle \boldsymbol{\varepsilon}_\alpha \rangle \cdot \bar{\mathbb{C}}[\langle \boldsymbol{\varepsilon}_\beta \rangle], \tag{19}$$

it is possible to determine the effective (homogeneous) stiffness $\bar{\mathbb{C}}$ by solving (10) for a basis of the six dimensional space of macroscopic strains $\bar{\boldsymbol{\varepsilon}}$. Hence, $\boldsymbol{\varepsilon}_\alpha$ or $\boldsymbol{\varepsilon}_\beta$, respectively, denote the six necessary linear independent loading cases with $\alpha, \beta \in \{1,\dots,6\}$. The same can be done for the effective compliance $\bar{\mathbb{S}}$

$$\frac{1}{2}\langle \boldsymbol{\sigma}_\alpha \cdot \mathbb{S}[\boldsymbol{\sigma}_\beta] \rangle = \frac{1}{2}\langle \boldsymbol{\sigma}_\alpha \rangle \cdot \bar{\mathbb{S}}[\langle \boldsymbol{\sigma}_\beta \rangle]. \tag{20}$$

By applying the results of Bishop and Hill (1951a,b), the effective stiffness and compliance can be obtained

$$\langle \mathbb{C}[\boldsymbol{\varepsilon}_\beta] \rangle = \bar{\mathbb{C}}[\langle \boldsymbol{\varepsilon}_\beta \rangle], \tag{21}$$

$$\langle \mathbb{S}[\boldsymbol{\sigma}_\beta] \rangle = \bar{\mathbb{S}}[\langle \boldsymbol{\sigma}_\beta \rangle]. \tag{22}$$

2.3.4. Lippmann–Schwinger equations for the Hashin–Shtrikman bounds

The energy principle of Hashin and Shtrikman (1962b) states that for any choice of the polarization field $\boldsymbol{p}(\boldsymbol{x})$, the following bounds on the elastic energy in the unit-cell hold true

$$\langle \boldsymbol{\varepsilon} \cdot \mathbb{C}[\boldsymbol{\varepsilon}] \rangle \underset{(\geqslant)}{\leqslant} \bar{\boldsymbol{\varepsilon}} \cdot \mathbb{C}_0[\bar{\boldsymbol{\varepsilon}}] + 2\langle \boldsymbol{p} \rangle \cdot \bar{\boldsymbol{\varepsilon}} - \left\langle \boldsymbol{p} \cdot (\mathbb{C} - \mathbb{C}_0)^{-1}[\boldsymbol{p}] \right\rangle - \langle \boldsymbol{p} \cdot (\mathbb{G}_0 * \boldsymbol{p}) \rangle, \tag{23}$$

if $\mathbb{C} \leqslant \mathbb{C}_0$ ($\mathbb{C} \geqslant \mathbb{C}_0$). Equality is reached when $\boldsymbol{p} = (\mathbb{C} - \mathbb{C}_0)[\boldsymbol{\varepsilon}]$. These bounds are applied to the subspace of voxel-wise constant polarization fields (Brisard and Dormieux, 2010). It is shown, that by introducing the periodized Green operator $\mathbb{G}_0^{\#}$, the bounds (23) or $\mathbb{G}_0 * \boldsymbol{p}$, respectively, can be calculated in this subspace without any approximation error by a discrete fast Fourier transformation. Since Willis (1977) has shown that the Hashin–Shtrikman bounds are quadratic positive (negative) definite forms on the space of all polarization fields, an optimal polarization field $\boldsymbol{p}^{\mathrm{HS}}$ in this subspace has to exist.

Please cite this article in press as: Müller, V., et al. Homogenization of linear elastic properties of short-fiber reinforced composites – A comparison of mean field and voxel-based methods. Int. J. Solids Struct. (2015), http://dx.doi.org/10.1016/j.ijsolstr.2015.02.030

Applying this result for the polarization fields to the associated strain field

$$\boldsymbol{\varepsilon}^{\mathrm{HS}} := (\mathbb{C} - \mathbb{C}_0)^{-1}[\boldsymbol{p}^{\mathrm{HS}}], \tag{24}$$

results in the following equation

$$\boldsymbol{\varepsilon}^{\mathrm{HS}} + \mathbb{G}_0^{\#} * \left((\mathbb{C} - \mathbb{C}_0)[\boldsymbol{\varepsilon}^{\mathrm{HS}}]\right) = \bar{\boldsymbol{\varepsilon}}, \tag{25}$$

which is of the same form as (16). This means, that the bounds of Hashin–Shtrikman can be calculated by the methods discussed for the strain based formulation of the Lippmann–Schwinger equation. The difficulties arising in the calculation of the periodized Green operator $\mathbb{G}_0^{\#}$ are discussed in Brisard and Dormieux (2010).

Equivalently, the stress based formulation of the Lippmann–Schwinger equation can be restated. This formulation has the advantage, that rigid inclusions can be treated without problems. Following Hill (1963), the eigenstrain $\varepsilon^{\star}$ is introduced:

$$\boldsymbol{\varepsilon}^{\star} = \mathbb{S}_0[\boldsymbol{p}] = (\mathbb{S}_0 - \mathbb{S})[\boldsymbol{\sigma}]. \tag{26}$$

This leads to the following formulation of the bounds of Hashin–Shtrikman (Willis, 1977)

$$\langle \boldsymbol{\sigma} \cdot \mathbb{S}[\boldsymbol{\sigma}] \rangle \underset{(\geqslant)}{\leqslant} \bar{\boldsymbol{\sigma}} \cdot \mathbb{S}_0[\bar{\boldsymbol{\sigma}}] + 2\langle \boldsymbol{\varepsilon}^{\star} \rangle \cdot \bar{\boldsymbol{\sigma}} + \left\langle \boldsymbol{\varepsilon}^{\star} \cdot (\mathbb{S} - \mathbb{S}_0)^{-1}[\boldsymbol{\varepsilon}^{\star}] \right\rangle + \left\langle \boldsymbol{\varepsilon}^{\star} \cdot \left(\mathbb{L}_0 * \boldsymbol{\varepsilon}^{\star}\right) \right\rangle, \tag{27}$$

if $\mathbb{C} \leqslant \mathbb{C}_0$ ($\mathbb{C} \geqslant \mathbb{C}_0$) or equivalently $\mathbb{S} \geqslant \mathbb{S}_0$ ($\mathbb{S} \leqslant \mathbb{S}_0$). Again, equality is reached for $\boldsymbol{\varepsilon}^{\star} = (\mathbb{S}_0 - \mathbb{S})[\boldsymbol{\sigma}]$. Applying the above arguments to the associated stress field $\boldsymbol{\sigma}^{\mathrm{HS}} := (\mathbb{S}_0 - \mathbb{S})^{-1}[\boldsymbol{\varepsilon}^{\star\mathrm{HS}}]$ of the optimal eigenstrain field $\boldsymbol{\varepsilon}^{\star\mathrm{HS}}$ in the subspace of voxel-wise constant eigenstrain fields, the following equation is obtained

$$\boldsymbol{\sigma}^{\mathrm{HS}}(\boldsymbol{x}) + \left(\mathbb{L}_0^{\#} * \left((\mathbb{S} - \mathbb{S}_0)[\boldsymbol{\sigma}^{\mathrm{HS}}]\right)\right)(\boldsymbol{x}) = \bar{\boldsymbol{\sigma}}, \tag{28}$$

with $\mathbb{L}_0^{\#}$ being the periodized Green operator for stresses which is defined in the same way as the periodized Green operator for strains.

2.3.5. Numerical algorithm

Both, the strain based formulation (16) as well as the stress based formulation (17) of the Lippmann–Schwinger equation can be iteratively solved using the Neumann series expansion for inverting the operator $\mathbb{I}^{s} + \mathbb{B}_{\varepsilon}$ or $\mathbb{I}^{s} + \mathbb{B}_{\sigma}$, respectively. The iterates of the local strain or stress, respectively, reads

$$\boldsymbol{\varepsilon}^{n} = \sum_{\alpha=0}^{n} (-\mathbb{B}_{\varepsilon})^{\alpha}[\bar{\boldsymbol{\varepsilon}}], \quad \boldsymbol{\sigma}^{n} = \sum_{\alpha=0}^{n} (-\mathbb{B}_{\sigma})^{\alpha}[\bar{\boldsymbol{\sigma}}], \tag{29}$$

which can also be written as

$$\boldsymbol{\varepsilon}^{0} = \bar{\boldsymbol{\varepsilon}}, \qquad \boldsymbol{\sigma}^{0} = \bar{\boldsymbol{\sigma}}, \tag{30}$$

$$\boldsymbol{\varepsilon}^{n+1} = -\mathbb{B}_{\varepsilon}[\boldsymbol{\varepsilon}^{n}] + \bar{\boldsymbol{\varepsilon}}, \quad \boldsymbol{\sigma}^{n+1} = -\mathbb{B}_{\sigma}[\boldsymbol{\sigma}^{n}] + \bar{\boldsymbol{\sigma}}. \tag{31}$$

The iterates (31) can be efficiently calculated in four simple steps using discrete fast Fourier transformation (DFT) by the so called basic scheme for polarization and eigenstrain, respectively (see Moulinec and Suquet, 1994):

$$\boldsymbol{p} = (\mathbb{C} - \mathbb{C}_0)[\boldsymbol{\varepsilon}^{n}], \qquad \boldsymbol{\varepsilon}^{\star} = (\mathbb{S} - \mathbb{S}_0)[\boldsymbol{\sigma}^{n}], \tag{32}$$

$$\hat{\boldsymbol{p}} = \mathrm{DFT}(\boldsymbol{p}), \qquad \hat{\varepsilon^{\star}} = \mathrm{DFT}(\boldsymbol{\varepsilon}^{\star}), \tag{33}$$

$$\hat{\boldsymbol{\varepsilon}^{\star}} = -\hat{\mathbb{G}}_0[\hat{\boldsymbol{p}}], \quad \hat{\boldsymbol{\varepsilon}^{\star}}(0) = \bar{\boldsymbol{\varepsilon}}, \qquad \hat{\boldsymbol{p}} = -\hat{\mathbb{L}}_0[\hat{\boldsymbol{\varepsilon}^{\star}}], \quad \hat{\boldsymbol{p}}(0) = \bar{\boldsymbol{\sigma}}, \tag{34}$$

$$\boldsymbol{\varepsilon}^{n+1} = \mathrm{DFT}^{-1}(\hat{\boldsymbol{\varepsilon}^{\star}}), \qquad \boldsymbol{\sigma}^{n+1} = \mathrm{DFT}^{-1}(\hat{\boldsymbol{p}}). \tag{35}$$

Previously defined in (26), in these equations, the sign of the eigenstrain $\boldsymbol{\varepsilon}^{\star}$ is changed, to get an identical algorithm for the strain and stress formulation. Expressions for $\hat{\mathbb{G}}_0$ can be found in Mura (1987) for different types of anisotropy.

The computation of the Hashin–Shtrikman bounds (25) and (28) can be done by replacing the Green operators $\mathbb{G}_0$ and $\mathbb{L}_0$ in the basic scheme with their periodized counterparts $\mathbb{G}_0^{\#}$ resp. $\mathbb{L}_0^{\#}$ (Brisard and Dormieux, 2010).

2.3.6. Hashin–Shtrikman bounds on the effective moduli

According to Kabel and Andrä (2013), it is possible to use the solutions of the Lippmann–Schwinger equations (25) and (28) to obtain upper and lower bounds on the effective moduli. Additionally, the assumptions in terms of the Hashin–Shtrikman bounds on $\mathbb{C}_0$ will have the consequence, that it is not possible to calculate an upper (lower) bound of the effective stiffness numerically, if the composite contains any rigid (porous) region. This is, however, not a real limitation, since in the first case, the upper Hashin–Shtrikman bound is a rigid material, and in the second case, the lower Hashin–Shtrikman bound is a material without any elastic stiffness. In the case of a composite having both rigid and porous regions, the assumptions of the Hashin–Shtrikman bounds cannot be fulfilled.

In appendix A is shown, that combining (19) and (21) with (23) yields

$$\bar{\boldsymbol{\varepsilon}} \cdot \bar{\mathbb{C}}[\bar{\boldsymbol{\varepsilon}}] = \bar{\boldsymbol{\varepsilon}} \cdot \mathbb{C}_{\boldsymbol{\varepsilon}}^{\mathrm{HS}}[\bar{\boldsymbol{\varepsilon}}]. \tag{36}$$

It follows

$$\mathbb{C} \underset{(\geqslant)}{\leqslant} \mathbb{C}_0 \Rightarrow \bar{\mathbb{C}} \underset{(\geqslant)}{\leqslant} \mathbb{C}_{\boldsymbol{\varepsilon}}^{\mathrm{HS}}. \tag{37}$$

Further in appendix A is shown, that combining (20) and (22) with (27) yields an analogous result for the compliance

$$\bar{\boldsymbol{\sigma}} \cdot \bar{\mathbb{S}}[\bar{\boldsymbol{\sigma}}] - \bar{\boldsymbol{\sigma}} \cdot \mathbb{S}_0[\bar{\boldsymbol{\sigma}}] = \bar{\boldsymbol{\sigma}} \cdot \left(\mathbb{S}_0 - \mathbb{S}_{\boldsymbol{\sigma}}^{\mathrm{HS}}\right)[\bar{\boldsymbol{\sigma}}]. \tag{38}$$

Therefore, if $\mathbb{S} \underset{(\leqslant)}{\geqslant} \mathbb{S}_0$

$$\bar{\mathbb{S}} \underset{(\geqslant)}{\leqslant} 2\mathbb{S}_0 - \mathbb{S}_{\boldsymbol{\sigma}}^{\mathrm{HS}} \underset{(\geqslant)}{\leqslant} 2\bar{\mathbb{S}} - \mathbb{S}_{\boldsymbol{\sigma}}^{\mathrm{HS}}, \tag{39}$$

which means that

$$\mathbb{S} \underset{(\leqslant)}{\geqslant} \mathbb{S}_0 \Rightarrow \mathbb{S}_{\boldsymbol{\sigma}}^{\mathrm{HS}} \underset{(\geqslant)}{\leqslant} \bar{\mathbb{S}}. \tag{40}$$

For non-rigid materials this implies

$$\mathbb{C} \underset{(\geqslant)}{\leqslant} \mathbb{C}_0 \Rightarrow \bar{\mathbb{C}} \underset{(\geqslant)}{\leqslant} \mathbb{C}_{\boldsymbol{\sigma}}^{\mathrm{HS}}. \tag{41}$$

From their convergence analysis, Michel et al. (2001) and Eyre and Milton (1999) concluded, that the convergence of the Neumann series expansion (29) for the strain based formulation of the Lippmann–Schwinger equation (25) is only guaranteed for $\mathbb{C} \leqslant \mathbb{C}_0$. The opposite is true for the stress based formulation, for which only $\mathbb{S} \leqslant \mathbb{S}_0$ guarantees the convergence of the Neumann expansion (29). To sum up, the strain (stress) based formulation allows the determination of an upper (lower) bound of the effective stiffness if the composite does not contain any rigid inclusion (pore space)

$$\mathbb{C}_{\boldsymbol{\sigma}}^{\mathrm{HS}} \leqslant \bar{\mathbb{C}} \leqslant \mathbb{C}_{\boldsymbol{\varepsilon}}^{\mathrm{HS}}. \tag{42}$$

3. Model microstructures and material parameters used for homogenization

3.1. Generation of model microstructures

The mean orientation distribution can be described with fabric tensors of second rank $\boldsymbol{N}$ (Kanatani, 1984), also called fiber

orientation tensors (Advani and Tucker, 1987). For N equal weighted fiber orientations $\boldsymbol{n}$, the orientation tensor is defined as

$$\boldsymbol{N} = \frac{1}{N}\sum_{\alpha=1}^{N} \boldsymbol{n}_\alpha \otimes \boldsymbol{n}_\alpha. \tag{43}$$

Since the fiber axis orientation $\boldsymbol{n}$ is normalized, the trace of the fiber orientation tensor is always one: $\mathrm{tr}(\boldsymbol{N}) = 1$.

Three different microstructures have been used for the comparison of the methods. Firstly, a microstructure with unidirectional aligned fibers has been considered. Results affiliated with this microstructure are referred to with UD in the following. Secondly, inspired by the orientation distribution of the fiber axes in injection-molded thin plates, two different microstructures with misaligned fiber axes have been considered. Results based on this microstructures are denoted with TP1 and TP2 (thin plate) in the following. All microstructures are generated under a periodicity constraint. In Table 2, the components of the orientation tensors, which have been used to generate the model microstructures, are given. The artificial microstructures have been generated by using GeoDict (2014). The corresponding data files can be found on the internet page http://www.itm.kit.edu/cm/288.php. The algorithm is described in Schladitz et al. (2006).

For all microstructures, the fibers have been modeled by cylinders with a length of $l = 200$ µm and a diameter of $d = 10$ µm. Ten different RVEs have been realized for each microstructure type. The side length of the RVEs has been $d_{\mathrm{RVE}} = 250$ µm, and they have been discretized with the resolutions $125, 250$ and 500, corresponding to a side length of one voxel of 2 µm, 1 µm, and 0.5 µm, in all directions for consideration in the full field approach. For all realizations, the fiber volume fraction is assumed to be equal to $c_{\mathrm{F}} = 13\%$. Additionally, for UD, fiber volume fractions of 17% and 21% have been taken into account. Since the mean field methods only rely on the orientation information, the explicit geometrical description of the orientation and geometry of each fiber is necessary. In Fig. 1, examples for UD and TP1 microstructures are given.

Table 2
Components of orientation tensors, used for the generation of the model microstructures.

	N_{11}	N_{22}	N_{33}	N_{23}	N_{13}	N_{12}
$\boldsymbol{N}_0^{\mathrm{TP1}}$	0.61	0.36	0.03	0.0	0.0	0.0
$\boldsymbol{N}_0^{\mathrm{TP2}}$	0.80	0.18	0.02	0.0	0.0	0.0
$\boldsymbol{N}_0^{\mathrm{UD}}$	1.0	0.0	0.0	0.0	0.0	0.0

3.2. Properties of the model microstructures

The microstructure generation process, which is implemented in GeoDict, is a random process. In the UD case, the microstructure generation algorithm matches perfectly the unidirectional alignment of the fibers. The achieved mean orientation tensors of the TP RVEs are compared with the target orientation tensors in Table 3.

3.3. Parameter overview

As mentioned above, three different microstructure types with three different fiber volume fractions have been regarded for the comparison of the homogenization methods. Additionally, three different combination of elastic moduli for fibers and matrix have been taken into account: First, the elastic moduli have been chosen corresponding to polypropylene ($E_{\mathrm{PP}} = 1.665$ GPa, $\nu_{\mathrm{PP}} = 0.36$) and glass ($E_{\mathrm{G}} = 73$ GPa, $\nu_{\mathrm{G}} = 0.2$) (Joshi et al., 1994; Tomasetti et al., 1998). These materials are frequently used to compound composites like PPGF30, consisting of polypropylene reinforced with glass fiber of a weight fraction of 30%. The phase contrast of this combination amounts to $\xi = 44$. Further, the phase contrast has been increased to 100 and 1000, whereby Young's modulus of the matrix and fibers is set to $E_{\mathrm{M}} = 1$ GPa and $E_{\mathrm{F}} = 100$ GPa or $E_{\mathrm{F}} = 1000$ GPa. The parameter variation is summarized in Table 4.

Table 3
Components of the average orientation tensors of 10 realization of the TP microstructures and their deviations compared with the target orientation tensors (see Table 2).

	N_{11}	N_{22}	N_{33}	N_{23}	N_{13}	N_{12}
$\bar{\boldsymbol{N}}^{\mathrm{TP1}}$	0.6083	0.3615	0.0302	0.0064	−0.0017	0.0004
$\boldsymbol{N}_0^{\mathrm{TP1}} - \bar{\boldsymbol{N}}^{\mathrm{TP1}}$	0.17%	−0.15%	1.02%	−0.64%	0.17%	−0.04%
$\bar{\boldsymbol{N}}^{\mathrm{TP2}}$	0.8058	0.1743	0.0199	−0.0006	0.0022	0.0114
$\boldsymbol{N}_0^{\mathrm{TP2}} - \bar{\boldsymbol{N}}^{\mathrm{TP2}}$	−0.58%	0.57%	0.01%	0.06%	−0.22%	−0.11%

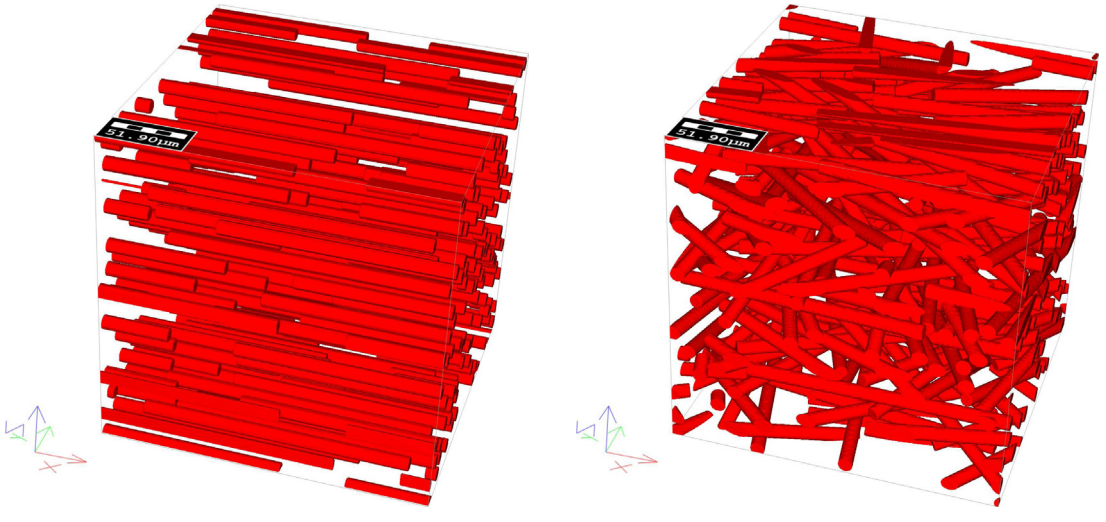

(a) (b)

Fig. 1. (a) UD microstructure; (b) TP microstructure.

Please cite this article in press as: Müller, V., et al. Homogenization of linear elastic properties of short-fiber reinforced composites – A comparison of mean field and voxel-based methods. Int. J. Solids Struct. (2015), http://dx.doi.org/10.1016/j.ijsolstr.2015.02.030

Table 4
Variation of microstructural and material parameters.

Microstructure	Fiber volume fraction		Material combination			
TP1	TP1/TP2	UD		$\xi = 44$	$\xi = 100$	$\xi = 1000$
TP2	13%	13%	E_F [GPa]	1.665	1	1
UD		17%	ν_F	0.36	0.36	0.36
		12%	E_M [GPa]	73	100	1000
			ν_M	0.36	0.36	0.36

4. Numerical results

4.1. Directional dependent elastic properties

To compare the effective stiffnesses, the directional dependent Young's modulus and bulk modulus can be evaluated. The directional dependent Young's modulus

$$\frac{1}{E(\boldsymbol{d})} = \boldsymbol{d} \otimes \boldsymbol{d} \cdot \bar{\mathbb{S}}[\boldsymbol{d} \otimes \boldsymbol{d}] \tag{44}$$

and the directional dependent bulk modulus

$$\frac{1}{3K(\boldsymbol{d})} = \boldsymbol{I} \cdot \bar{\mathbb{S}}[\boldsymbol{d} \otimes \boldsymbol{d}] \tag{45}$$

determine uniquely the effective compliance tensor $\bar{\mathbb{S}} = \bar{\mathbb{C}}^{-1}$ (see, e.g., Böhlke and Brüggemann, 2001). In Fig. 2, the graphical representations of these quantities are given exemplarily for a UD realization. In the following, the numerical results are compared by means of the directional dependent Young's modulus. on the one hand, a quarter of the contour of this quantity is shown on the x–y-plane. Here, this plane is the plane with the main fiber orientation distribution in terms of UD and TP. On the over hand, the comparison is expressed by means of a relative deviation of the directional dependent Young's modulus of method X and Y:

$$\eta_{\mathrm{Y}}^{\mathrm{X}} = \left(\frac{\int_S \left(E^{\mathrm{X}}(\boldsymbol{n}) - E^{\mathrm{Y}}(\boldsymbol{n})\right)^2 \mathrm{d}S}{\int_S \left(E^{\mathrm{X}}(\boldsymbol{n})\right)^2 \mathrm{d}S} \right)^{1/2}. \tag{46}$$

4.2. Resolution, size and realization dependency of Young's modulus

4.2.1. Spatial resolution of RVE

In order to evaluate the dependencies of the FFT solution on the resolution, Young's moduli have been calculated in 0°-direction (E_0) for each realization of the three different resolutions for two different phase contrasts, $\xi = 44$ and $\xi = 1000$. For UD microstructures with a volume fraction of 13%, these results are shown in Fig. 3, and, for TP1 microstructures in Fig. 4. In both figures, the mean Young's modulus values and the corresponding standard deviation of all realizations for the lower bound (FFT-HS−), the basic scheme (FFT-BS), and the upper bound (FFT-HS+) in the appropriate direction are shown.

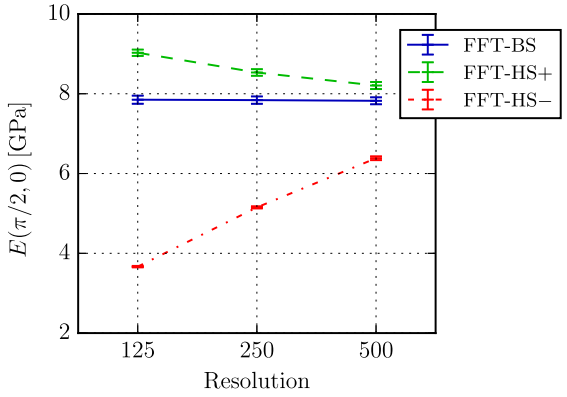

(a) UD with $c_F = 13\%$ and $\xi = 44$

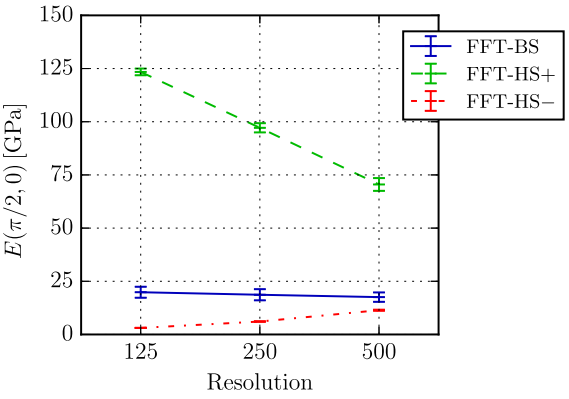

(b) UD with $c_F = 13\%$ and $\xi = 1000$

Fig. 3. Mean Young's modulus and standard deviation in 0°-direction of UD microstructure realizations in dependence of the resolution of the RVE for FFT methods.

Since the averaged Young's modulus values of the FFT-BS solution are on an approximately constant level for both microstructure types, a dependency on the resolution cannot be observed. The standard deviation of the FFT-BS results in terms of different RVE realizations is similar for all resolutions. Contrary to this, FFT-HS+ and FFT-HS− dependent obviously on the resolution: the gap between the corresponding bounds is narrowed with increasing resolution. This can be reasoned with an increasing space for solution in this case of voxel-wise constant field variables. Thus, tighter bounds can be found based on Eq. (27). For the smaller phase contrast of $\xi = 44$, FFT-HS+ is closer and converges faster to FFT-BS for UD and TP1 in the considered direction. Just the opposite can be observed for the larger phase contrast of

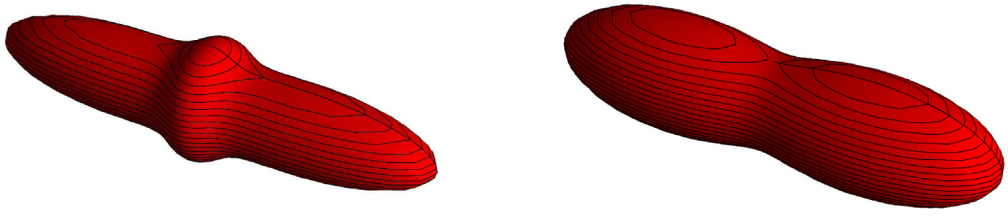

(a) (b)

Fig. 2. Graphical representation of the directional dependent (a) Young's modulus and (b) bulk modulus for one UD realization.

Please cite this article in press as: Müller, V., et al. Homogenization of linear elastic properties of short-fiber reinforced composites – A comparison of mean field and voxel-based methods. Int. J. Solids Struct. (2015), http://dx.doi.org/10.1016/j.ijsolstr.2015.02.030

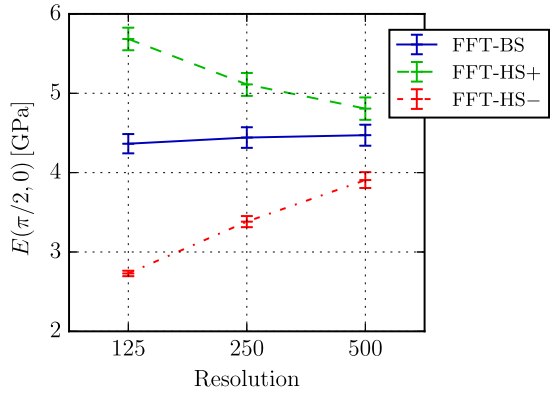

(a) TP1 with $c_F = 13\%$ and $\xi = 44$

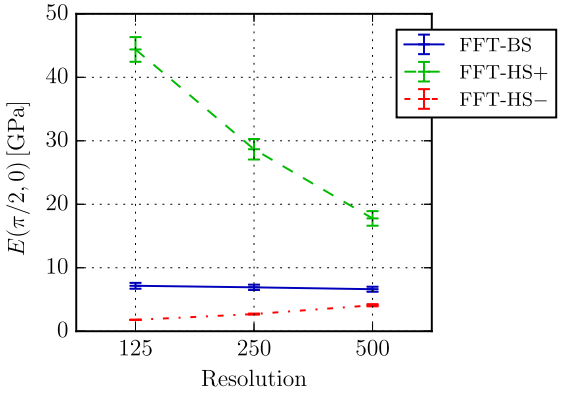

(b) TP1 with $c_F = 13\%$ and $\xi = 1000$

Fig. 4. Mean Young's modulus and standard deviation in 0°-direction of TP1 microstructure realizations in dependence of the resolution of the RVE for FFT methods.

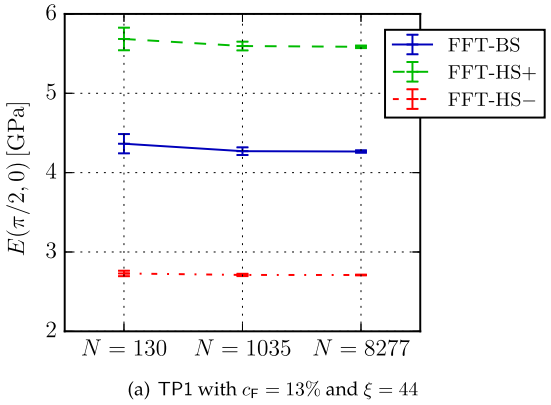

(a) TP1 with $c_F = 13\%$ and $\xi = 44$

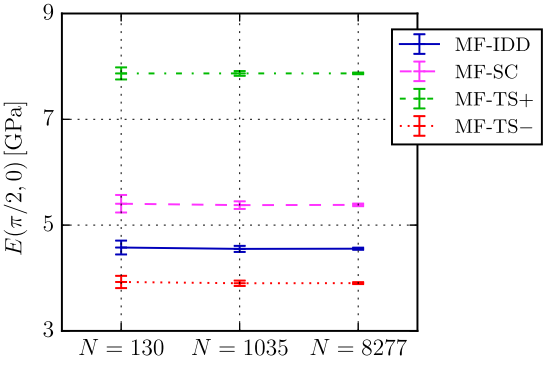

(b) TP1 with $c_F = 13\%$ and $\xi = 44$

Fig. 5. Mean Young's modulus and standard deviation of TP1 microstructure realizations in 0°-direction in dependence of the size of the RVE for (a) FFT methods and (b) MF approaches.

$\xi = 1000$. The standard deviation of FFT-HS+ is slightly increasing for UD with $\xi = 44$ and obviously increasing for UD with $\xi = 1000$. In the TP1 case, its standard deviation is approximately constant for the smaller phase contrast and decreasing for the larger phase contrast. The standard deviation of FFT-HS− increases in all cases with increasing resolution.

4.2.2. Size of RVE

In order to verify the representativity of the volume element for the misaligned microstructure configuration, additional volume elements of three different sizes have been considered for TP1: Starting with 250 µm, the side length has been doubled two times to 500 μm and 1000 µm. Again, ten volume elements with a resolution of 125, 250 and 500 voxels, respectively, in each direction have been generated and homogenized using the FFT and MF methods. The resulting averaged Young's modulus in 0°-direction and its standard deviation are shown in Fig. 5(a) for the FFT and in Fig. 5(b) for the MF approaches.

Despite the low resolution which has been chosen due to computational issues, it is obvious from Fig. 5, that the mean values of Young's modulus are approximately constant for all RVE sizes. The FFT and MF methods show qualitatively comparable results in Fig. 5(a) and in Fig. 5(b), respectively. On the one hand, for small RVEs with 130 inclusions, a dependency on the specific realization is evident. On the other hand, for the midsize and large volume elements with 1035 and 8277 inclusions, respectively, Young's modulus does not show a significant dependency on a specific realization. The correspondence of the orientation distribution in terms of the fiber orientation tensor compared to the target given in Table 2 is the better, the larger the volume elements become, see Table 5. Since the mean stiffnesses and also the mean direction-dependent Young's modulus are constant regarding different RVE sizes, it is concluded, that the representativity is also given for the small RVEs in an averaged manner.

4.2.3. Variation in RVE generation

The variation of the microstructure realization process is analyzed by means of averaged directional dependent Young's moduli and standard deviations of all realizations on the x–y-plane. In Fig. 6 and 7, FFT results are shown for UD and TP1, respectively. In each figure, results for microstructures with a fiber volume fraction of 13% and a phase contrast of 44 and 1000 are presented. Especially for UD, a direction dependence of the standard deviation of Young's modulus can be observed: The greatest deviation occurs in fiber direction (0°-direction) and the smallest in transversal direction for all FFT methods. It increases for higher averaged Young's modulus. Thus, for the upper bound FFT-HS+ and for larger phase contrast the greatest standard deviation is found. However, relating the standard deviation to the averaged Young's

Table 5
Components of orientation tensors of RVEs with an endge-length of 250 µm, 500 µm and 1000 µm.

	N_{11}	N_{22}	N_{33}	N_{23}	N_{13}	N_{12}
$\boldsymbol{N}_{130}^{TP1}$	0.6086	0.3614	0.0299	0.0062	−0.0020	0.0014
$\boldsymbol{N}_{1035}^{TP1}$	0.6115	0.3581	0.0304	−0.0005	0.0007	−0.0007
$\boldsymbol{N}_{8277}^{TP1}$	0.6113	0.3586	0.0301	0.0000	−0.0001	−0.0003

Please cite this article in press as: Müller, V., et al. Homogenization of linear elastic properties of short-fiber reinforced composites – A comparison of mean field and voxel-based methods. Int. J. Solids Struct. (2015), http://dx.doi.org/10.1016/j.ijsolstr.2015.02.030

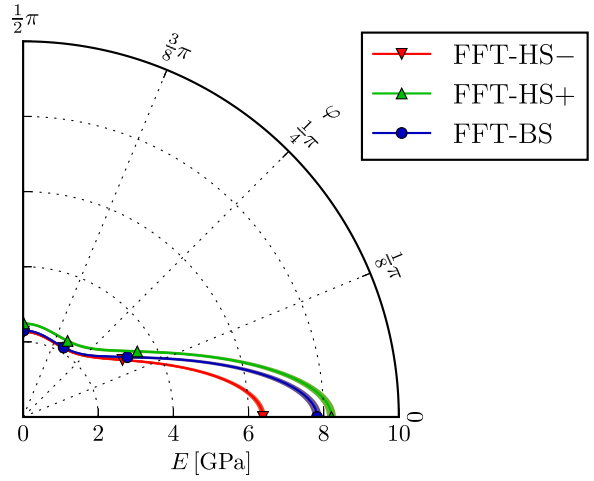

(a) UD with $c_F = 13\%$ and $\xi = 44$

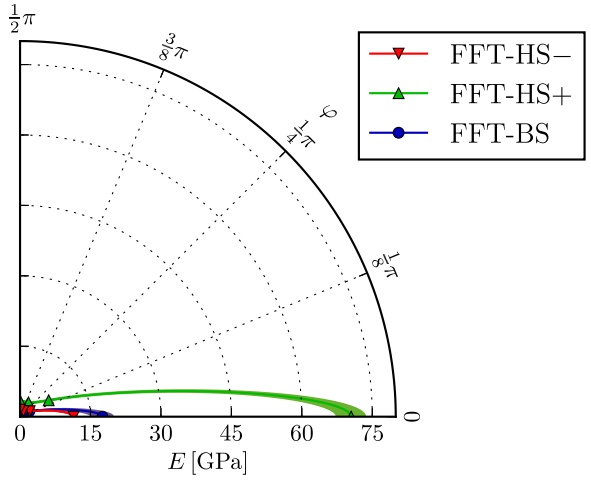

(b) UD with $c_F = 13\%$ and $\xi = 1000$

Fig. 6. Direction dependent Young's modulus and standard deviation in x–y-plane for UD microstructure realizations for FFT methods.

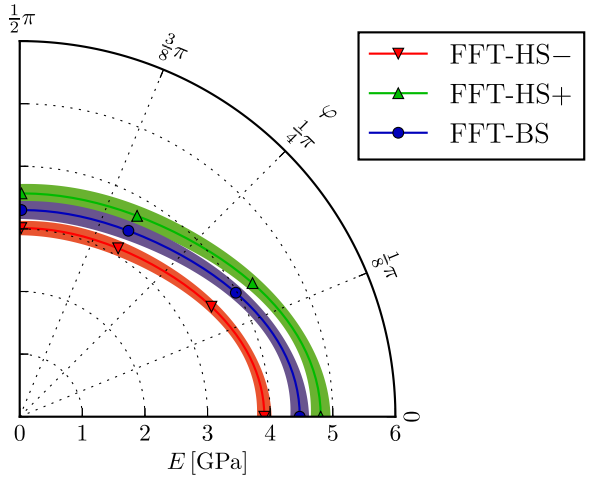

(a) TP1 with $c_F = 13\%$ and $\xi = 44$

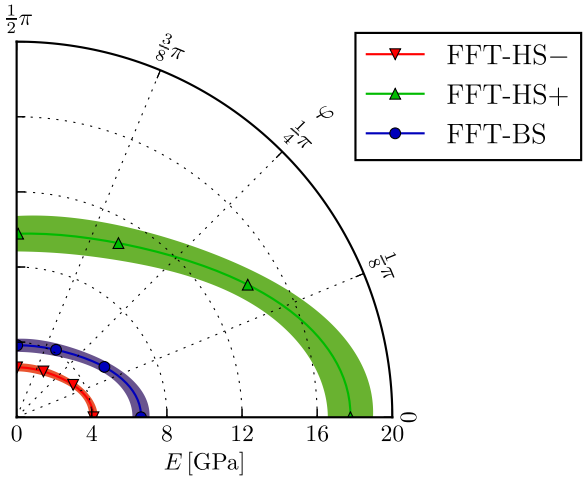

(b) TP1 with $c_F = 13\%$ and $\xi = 1000$

Fig. 7. Direction dependent Young's modulus and standard deviation in x–y-plane for TP1 microstructure realizations for FFT methods.

modulus in the corresponding direction reveals two facts: The greatest relative deviation of approximately 2% for $\xi = 44$ and 25% for $\xi = 1000$ occurs again in fiber direction but now for FFT-BS. Since the UD alignment is perfectly matched in all RVE realizations, no deviations can be observed in the MF results.

In the TP1 case in Fig. 7, no distinct direction dependence of the standard deviation can be observed for FFT results. However, the greatest deviations occur for methods delivering the greatest Young's modulus. If the standard deviation is related to the averaged Young's modulus, a deviation of 8% for $\xi = 44$ and 18% for $\xi = 1000$ is found. The MF results also depend on the RVE realization in the TP1 case, see Fig. 8. Here, again, no distinct direction dependence of the standard deviation can be observed. MF-SC delivers the highest sensitivity on specific RVE realizations and, thus, the highest standard deviation, also compared to FFT methods: 11% for $\xi = 44$ and 25% for $\xi = 1000$.

4.2.4. Effects of the periodicity constraint

For the generation of the TP microstructures, a periodicity constraint has been imposed. In order to quantify the effect of the periodicity, non-periodic TP1 RVEs with the side length of 250, 500 and 1000 µm have been generated additionally. Although the RVEs are not periodic, it is still possible to solve the boundary value problem using the FFT approaches with periodic boundary conditions. Compared to the results of FFT-BS for periodic microstructures, the relative deviation, which is defined in Eq. (46), decreases with increasing RVE side length of the non-periodic microstructures. For 250 µm the deviation amounts to 9.0%, for 500 µm to 6.7% and for the largest RVE with 1000 µm to 4.8%. The periodicity constraint ensures a constant fiber length, however, this is not the case for the non-periodic RVEs, which contain shorter fiber ends at their boundaries. Since the volume fraction of the short fiber ends decreases for increasing RVE size, the results are reasonable.

4.3. Deviation of Young's modulus

In the following, FFT-BS is compared with MF-IDD and MF-SC by means of a relative deviation defined in Eq. (46). Herein, the highest resolution of the RVEs have been used for FFT-BS. The effective averaged Young's moduli of the mentioned methods are compared for all microstructure types, phase contrasts and fiber volume fractions. For each comparison, the relative deviation has been calculated and shown in a heat map, see, e.g., Fig. 9. Herein, the relative deviation is entered directly on the one hand, and represented in color in order to see the tendencies better on the other hand.

Please cite this article in press as: Müller, V., et al. Homogenization of linear elastic properties of short-fiber reinforced composites – A comparison of mean field and voxel-based methods. Int. J. Solids Struct. (2015), http://dx.doi.org/10.1016/j.ijsolstr.2015.02.030

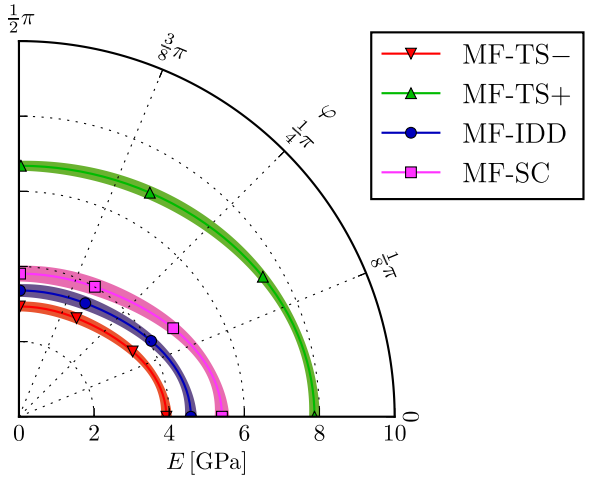

(a) TP1 with $c_F = 13\%$ and $\xi = 44$

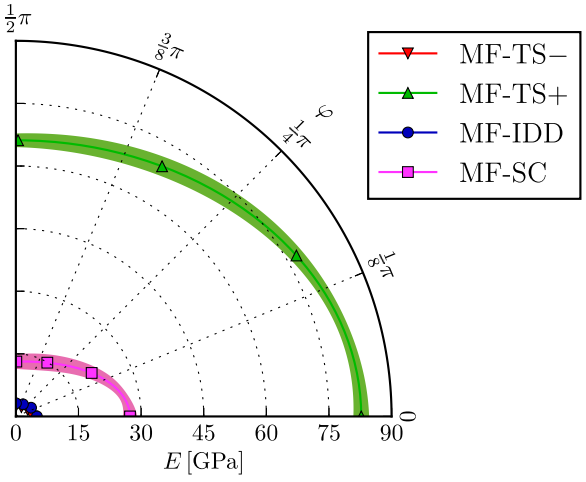

(b) TP1 with $c_F = 13\%$ and $\xi = 1000$

Fig. 8. Direction dependent Young's modulus and standard deviation in x–y-plane for TP1 microstructure realizations for MF methods.

In Fig. 9(a), first, FFT-BS and MF-IDD are compared for all microstructure types and phase contrasts. The smallest deviation of 1.5% occurs for TP1 with the smallest phase contrast $\xi = 44$. The largest deviation of 31.8% is found for UD with $\xi = 1000$. The deviation increases with increasing phase contrast and with advancing alignment of the fibers (TP1 → TP2 → UD). Similar results can be seen in Fig. 9(c), where FFT-BS and MF-IDD are compared for UD microstructures with all considered phase contrasts and volume fractions. Starting from 3%, the deviation increases with increasing phase contrast and also with increasing volume fraction up to 49.5%.

The relative deviation between MF-SC and FFT-BS for UD, shown in Fig. 9(d), reveal the same tendencies as MF-IDD and FFT-BS. Again, the deviation increases with increasing fiber volume fraction and phase contrast. The minimum and maximum deviations amount to 4.5% and 29.2%, respectively. Another tendency can be observed for the comparison of MF-SC and FFT-BS in terms of different microstructure types, see Fig. 9(b). Here, the deviation still increases with increasing phase contrast, however, it decreases with advancing alignment of the fibers.

The direct comparison of Young's modulus for TP2 with $c_F = 13\%$ and $\xi = 100$ is shown in Fig. 10(a) on the x–y-plane for all MF and FFT methods. Accordingly, in Fig. 10(b), the UD results of all methods are compared for $c_F = 17\%$ and $\xi = 100$. It can be seen, that the results of all methods are located between MF-TS+ and FFT-HS−, where FFT-BS appears between the narrow FFT bounds. MF-SC predicts a higher Young's modulus than FFT-BS and a partially higher Young's modulus than FFT-HS+, especially in fiber direction in the UD case. MF-IDD is located between FFT-BS and the lower bound FFT-HS−. In the UD case, MF-IDD and MF-TS− coincide for all parameters and appear between FFT-BS and FFT-HS−. MF-TS+ predicts a much higher Young's modulus then all other methods, additionally for UD, the shape of the MF-TS+ Young's modulus is different compared to the other approaches.

4.3.1. Effects of the ellipsoidal approximation of the cylindrical fibers

Generally, it is known that for UD, the effective material behavior in fiber direction is getting stiffer with increasing fiber length. The MF results discussed so far are based on the modeling of the cylindrical fibers by ellipsoids of equal aspect ratio and volume. Thus, the ellipsoids are longer than the cylindrical fibers in the RVE. The half axes of the ellipsoid, a_1, a_2 and a_3 are scaled by $(3/2)^{1/3}$:

$$2a_1 = \left(\frac{3}{2}\right)^{1/3} l, \quad 2a_2 = 2a_3 = \left(\frac{3}{2}\right)^{1/3} d,$$

where l and d are the length and the diameter of the cylindrical fiber. Alternatively, the cylindrical fibers can also be approximated by ellipsoids with the side condition of equal length and equal volume. Herein, the second and third half axis have to be scaled with $(3/2)^{1/2}$, while the first is exactly $2a_1 = l$. In Fig. 11, both approximations are shown for a fiber with an aspect ratio of 20. The ellipsoidal approximation with equal volume and aspect ratio overestimates the length and the width of the cylinder by about 14.5%, while the approximation with equal volume and equal length overestimates the width by 22.5%. In the following, these two approaches to model the cylindrical fibers by ellipsoids are distinguished by the terms first type ellipsoid and second type ellipsoid.

To determine the effect of the ellipsoidal approximation on the effective material properties, additional RVEs with unidirectional aligned first type ellipsoids and a fiber volume fraction of $c_F = 13\%$ have been generated. In Fig. 12, the relative differences between the averaged stiffnesses of the RVEs with cylindrical inclusions and ellipsoidal inclusions for FFT-BS, FFT-HS+ and FFT-HS− are shown for the phase contrast of 44 . In this figure, that error is indicated, which is introduced if the cylindrical fibers are modeled by first type ellipsoids. In the fiber direction, the difference ranges between 4% in case of FFT-BS and FFT-HS−, and 5% in case of FFT-HS+.

Using the second type ellipsoid for MF-SC and MF-IDD approaches, denoted by MF-SC2 and MF-IDD2, again an analysis of the relative deviation to FFT-BS with cylindrical inclusions have been performed. The results of this analysis is shown in Fig. 13. Compared with the former deviation analysis shown in Fig. 9, it can be seen, that the tendencies remain the same. However, all deviations of the comparison of MF-IDD2 and FFT-BS are higher than the deviations between MF-IDD and FFT-BS. The contrary is the case for MF-SC2 and FFT-BS: Here, the deviation are smaller than in the former analysis. This can be reasoned by the smaller aspect-ratio of the second type ellipsoidal approximation. Generally, MF-IDD predicts smaller Young's moduli than FFT-BS. Smaller aspect-ratios lead to smaller Young's moduli and, therefore, the deviations become larger. In case of MF-SC, which generally predicts larger Young's moduli than FFT-BS, the deviations become smaller for smaller aspect-ratios of the inclusions.

Please cite this article in press as: Müller, V., et al. Homogenization of linear elastic properties of short-fiber reinforced composites – A comparison of mean field and voxel-based methods. Int. J. Solids Struct. (2015), http://dx.doi.org/10.1016/j.ijsolstr.2015.02.030

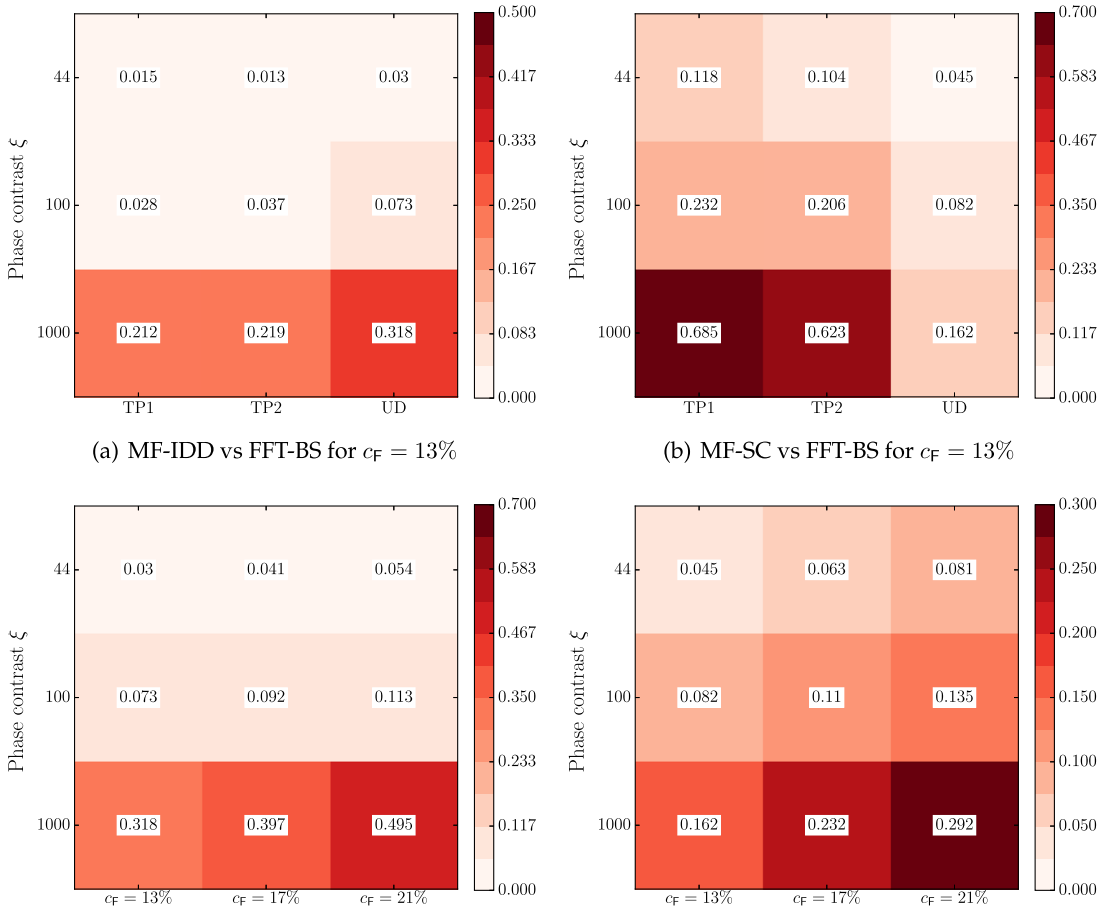

(a) MF-IDD vs FFT-BS for $c_F = 13\%$

(b) MF-SC vs FFT-BS for $c_F = 13\%$

(c) MF-IDD vs FFT-BS for UD

(d) MF-SC vs FFT-BS for UD

Fig. 9. Relative deviation of FFT-BS and (a) MF-IDD for TP1, TP2 and UD with $c_F = 13\%$, (b) MF-SC for TP1, TP2 and UD with $c_F = 13\%$, (c) MF-IDD for UD with $c_F = 13, 17, 21\%$ and (d) MF-SC for UD with $c_F = 13, 17, 21\%$.

5. Summary and conclusions

The main objective of this paper is the detailed comparison of the predicted effective linear elastic properties of full field and mean field methods for discontinuous short-fiber reinforced composites. For this purpose, the IDD scheme, the SC method and a TS approach, on the one hand, and a full field solution based on fast Fourier transformation, on the other hand, have been applied. In the case of the mean field methods, an explicit geometrical description of the fibers in terms of their geometrical properties can be taken into account. Whereas for the full field method, a regular three-dimensional discretization of the microstructures with voxel-wise constant properties is additionally necessary. The explicit description of the microstructures is available online. The properties of the considered microstructures have been analyzed. Three different types of microstructures have been considered, two misaligned and one unidirectional configuration, in conjunction with three phase contrasts, the smallest contrast of 44 for a PPGF composite and two artificial of 100 and 1000. Three different fiber volume fractions have been taken into account for the unidirectional configuration: 13%, 17% and 21%, what corresponds to weight fractions of 30%, 40% and 50% for the PPGF composite material. The numerical solutions have been compared in terms of the directional dependent Young's modulus regarding the dependency on resolution and size of the RVEs, the relative deviations of Young's modulus, and the anisotropy of Young's modulus in the plane of the main fiber orientation distribution.

In the following, the term *Young's modulus* always refers to the realization averaged Young's modulus. The term *specific Young's modulus* denotes Young's modulus of one particular RVE realization.

With respect to the model microstructures and their discretization, the following can be concluded:

- The range of Young's modulus between the upper and lower HS bounds of the FFT solution depends on the resolution (voxel) of the RVE. With increasing resolution, both bounds converge to the FFT-BS solution. The Young's modulus of the FFT-BS solution does not show an obvious dependency on the selected resolution of the RVE.
- No significant effect of the size of the RVE on Young's modulus of the TP configuration has been observed. While for small RVEs with 130 fibers, the specific Young's modulus depends on the realization, this is not the case for larger RVEs with 1035 and more fibers.
- In the UD case, the standard deviation of specific Young's moduli of FFT solutions show a dependency on a particular realization only in fiber direction. The deviation is higher for higher effective Young's moduli. The highest relative deviation, where the standard deviation is divided by the average Young's

Please cite this article in press as: Müller, V., et al. Homogenization of linear elastic properties of short-fiber reinforced composites – A comparison of mean field and voxel-based methods. Int. J. Solids Struct. (2015), http://dx.doi.org/10.1016/j.ijsolstr.2015.02.030

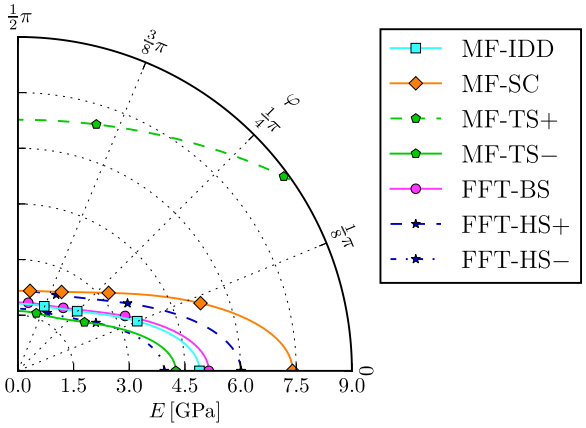

(a) TP2 with $c_F = 13\%$ and $\xi = 100$

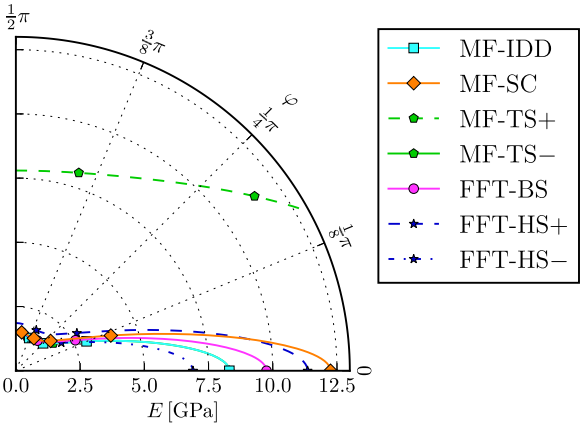

(b) UD with $c_F = 17\%$ and $\xi = 100$

Fig. 10. Direction dependent Young's modulus of all FFT and MF methods on *x*-*y*-plane.

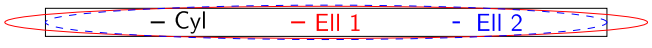

Fig. 11. Approximation of a cylindrical fiber with equal volume and aspect ratio or volume and length.

modulus, occurs for FFT-BS: 2% for a phase contrast of 44 and 25% for a phase contrast of 1000. No deviations occur for MF approaches.

- In the TP1 case, no distinct direction dependency of the standard deviation of specific Young's moduli can be observed. The SC method shows the highest sensitivity on the specific RVE realization. The relative standard deviation amounts to 11 and 25% for a phase contrast of 44 and 1000, respectively.

Thus, an RVE with a side length of 250 µm is sufficient for the considered microstructure with a constant fiber length of 200 µm, especially by means of averaged stiffnesses.

The comparison of the effective elastic properties predicted by the different homogenization schemes yields the following results:

- The comparison of FFT-BS and MF-IDD by means of a relative deviation of Young's modulus reveals the following tendencies for all considered microstructures with a fiber volume fraction of 13%: the relative deviation increases with increasing phase contrast and advancing alignment of the fibers. The relative deviation varies between 1.5% and 31.8%.
- In case of UD microstructures, the deviation of FFT-BS and MF-IDD increases with increasing phase contrast and with increasing fiber volume fraction. It varies between 3% and 49.5%.
- The relative deviation between FFT-BS and MF-SC shows another tendency for microstructures with a fiber volume fraction of 13%: It increases with increasing phase contrast but decreases with advancing alignment of the fibers. The relative deviation varies between 4.5% and 68.5%.
- For UD microstructures, the deviation between FFT-BS and MF-SC again increases with increasing phase contrast and with increasing fiber volume fraction. The relative deviation varies between 4.5% and 29.2%.
- If the cylindrical fibers are approximated with ellipsoids not under the conditions of equal aspect-ratio and volume, but, of equal length and volume, the tendencies of the relative deviations between MF and FFT approaches remain the same. However, it affects the comparison of FFT-BS and FFT-IDD in such way, that the deviations become slightly larger. In the comparison of FFT-BS with FFT-SC the deviation become slightly smaller.

Hence, under the assumption of first type ellipsoids in the MF approaches, quantitatively similar results of FFT-IDD and MF-BS approaches, i.e., a maximum relative deviation of 10%, are obtained for all considered microstructure types with a maximum phase contrast of 100 and a maximum fiber volume fraction of 17%. In the case of MF-SC and FFT-BS, only UD microstructures with a maximum phase contrast of 44 deliver a deviation, which suits to this condition. If second type ellipsoids are assumed for MF approaches, the relative deviation between FFT-BS and MF-IDD2 is smaller than 10% only for microstructures with a phase contrast of 44. The same is valid for the comparison of FFT-BS and MF-SC. Additionally, in the last comparison the UD microstructures with $c_F = 13\%$ for all considered phase contrast and $c_F = 17\%$ for $\xi = 100$ deliver small deviations.

The effect of the geometrical fiber modeling assumptions on the effective elastic properties can be summarized as follows:

- Apart from the volume fraction, the geometrical shape of the inclusions significantly affects the effective elastic properties predicted by the mean field and the full field approaches. The FFT-BS solution predicts a deviation of the effective

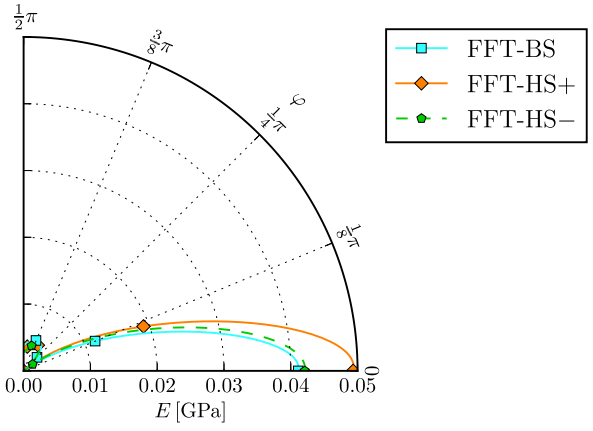

Fig. 12. Relative deviation of the directional dependent Young's modulus $\left|E^X_{cyl}(\varphi) - E^X_{ell}(\varphi)\right| / E^X_{cyl}(\varphi)$ for UD with $c_F = 13\%$ and $\xi = 44$ of the FFT methods for ellipsoidal and cylindrical inclusion geometry.

Please cite this article in press as: Müller, V., et al. Homogenization of linear elastic properties of short-fiber reinforced composites – A comparison of mean field and voxel-based methods. Int. J. Solids Struct. (2015), http://dx.doi.org/10.1016/j.ijsolstr.2015.02.030

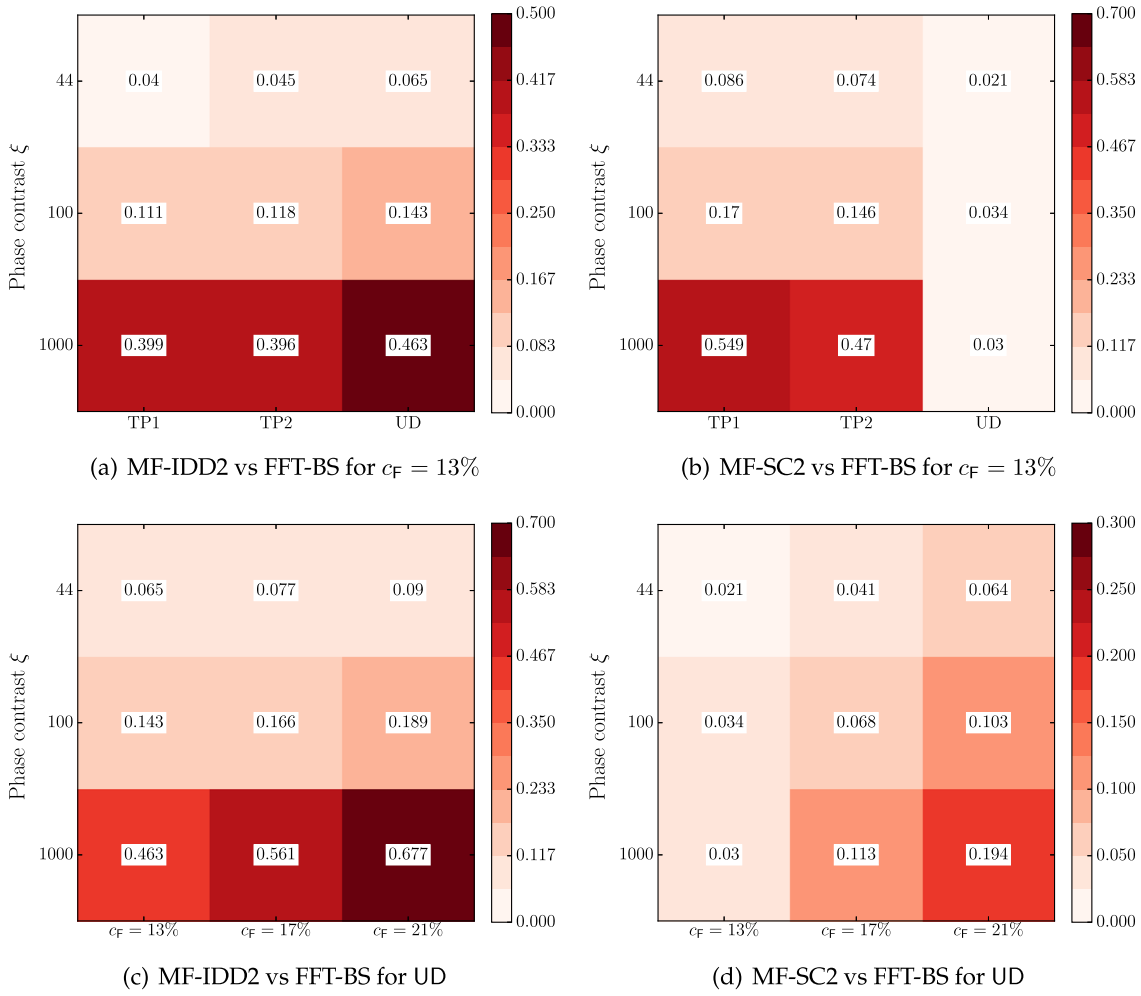

(a) MF-IDD2 vs FFT-BS for $c_F = 13\%$

(b) MF-SC2 vs FFT-BS for $c_F = 13\%$

(c) MF-IDD2 vs FFT-BS for UD

(d) MF-SC2 vs FFT-BS for UD

Fig. 13. Relative deviation of FFT-BS and (a) MF-IDD2 for TP1, TP2 and UD with $c_F = 13\%$, (b) MF-SC2 for TP1, TP2 and UD with $c_F = 13\%$, (c) MF-IDD2 for UD with $c_F = 13, 17, 21\%$ and (d) MF-SC2 for UD with $c_F = 13, 17, 21\%$.

Young's modulus in fiber orientation of 5% for the UD microstructures with a fiber volume fraction of 13% if cylindrical fibers are replaced with ellipsoidal approximations of equal aspect ratio.

Hence the shape of the inclusions affect the prediction of the effective elastic properties.

Altogether, it can be concluded, that the selection of the appropriate homogenization method should be done with regard to the problem at hand. The presented mean field approaches are numerically less expensive than the full field FFT method. On the one hand, this property allows to handle an equivalent amount of discrete microstructure datasets in shorter time or, on the other hand, to consider more expanded data like segmented microstructure data experimentally measured through micro-computer tomography. The presented FFT method is able to account for more complex geometrical characteristics, like long curved fibers, than the discussed mean field approaches. Additionally, the full field approach is numerically more efficient than other established full field methods like, e.g., FEM.

Acknowledgment

The research documented in this manuscript was partially initiated by the German–Canadian research group "Integrated engineering of continuous-discontinuous long fiber reinforced polymer structures". The support of the Institute of Engineering Mechanics at KIT by the German Research Foundation (DFG) is gratefully acknowledged.

Appendix A. Hashin–Shtrikman bounds on effective moduli

Combining (19) and (21) with (23) yields

$$\begin{aligned}
&\bar{\boldsymbol{\varepsilon}} \cdot \bar{\mathbb{C}}[\bar{\boldsymbol{\varepsilon}}] \\
&= \langle \boldsymbol{\varepsilon} \cdot \mathbb{C}[\boldsymbol{\varepsilon}] \rangle \\
&\underset{(\geqslant)}{\leqslant} \bar{\boldsymbol{\varepsilon}} \cdot \mathbb{C}_0[\bar{\boldsymbol{\varepsilon}}] + 2\langle \boldsymbol{p}^{HS} \rangle \cdot \bar{\boldsymbol{\varepsilon}} - \left\langle \boldsymbol{p}^{HS} \cdot (\mathbb{C} - \mathbb{C}_0)^{-1}[\boldsymbol{p}^{HS}] \right\rangle - \langle \boldsymbol{p}^{HS} \cdot (\mathbb{G}_0 * \boldsymbol{p}^{HS}) \rangle \\
&= \bar{\boldsymbol{\varepsilon}} \cdot \mathbb{C}_0[\bar{\boldsymbol{\varepsilon}}] + 2\langle \boldsymbol{p}^{HS} \rangle \cdot \bar{\boldsymbol{\varepsilon}} - \langle \boldsymbol{p}^{HS} \cdot \boldsymbol{\varepsilon}^{HS} \rangle - \langle \boldsymbol{p}^{HS} \cdot (\bar{\boldsymbol{\varepsilon}} - \boldsymbol{\varepsilon}^{HS}) \rangle \qquad (47) \\
&= \bar{\boldsymbol{\varepsilon}} \cdot \mathbb{C}_0[\bar{\boldsymbol{\varepsilon}}] + \langle \boldsymbol{p}^{HS} \rangle \cdot \bar{\boldsymbol{\varepsilon}} \\
&= \bar{\boldsymbol{\varepsilon}} \cdot \langle \mathbb{C}[\boldsymbol{\varepsilon}^{HS}] \rangle \\
&= \bar{\boldsymbol{\varepsilon}} \cdot \mathbb{C}_{\boldsymbol{\varepsilon}}^{HS}[\bar{\boldsymbol{\varepsilon}}].
\end{aligned}$$

Combining (20) and (22) with (27) yields an analogous result for the compliance

$$
\begin{aligned}
&\bar{\boldsymbol{\sigma}} \cdot \bar{\mathbb{S}}[\bar{\boldsymbol{\sigma}}] - \bar{\boldsymbol{\sigma}} \cdot \mathbb{S}_0[\bar{\boldsymbol{\sigma}}] \\
&= \langle \boldsymbol{\sigma} \cdot \mathbb{S}[\boldsymbol{\sigma}] \rangle - \bar{\boldsymbol{\sigma}} \cdot \mathbb{S}_0[\bar{\boldsymbol{\sigma}}] \\
&\underset{(\geqslant)}{\leqslant} 2\left\langle \boldsymbol{\varepsilon}^{\star\,\mathrm{HS}} \right\rangle \cdot \bar{\boldsymbol{\sigma}} + \left\langle \boldsymbol{\varepsilon}^{\star\,\mathrm{HS}} \cdot (\mathbb{S} - \mathbb{S}_0)^{-1}[\boldsymbol{\varepsilon}^{\star\,\mathrm{HS}}] \right\rangle + \left\langle \boldsymbol{\varepsilon}^{\star\,\mathrm{HS}} \cdot \left(\mathbb{L}_0 * \boldsymbol{\varepsilon}^{\star\,\mathrm{HS}} \right) \right\rangle \\
&= 2\left\langle \boldsymbol{\varepsilon}^{\star\,\mathrm{HS}} \right\rangle \cdot \bar{\boldsymbol{\sigma}} - \left\langle \boldsymbol{\varepsilon}^{\star\,\mathrm{HS}} \cdot \boldsymbol{\sigma}^{\mathrm{HS}} \right\rangle + \left\langle \boldsymbol{\varepsilon}^{\star\,\mathrm{HS}} \cdot (\mathbb{C}_0 - \mathbb{C}_0\mathbb{G}_0\mathbb{C}_0) * \left(\mathbb{S}_0[\boldsymbol{p}^{\mathrm{HS}}] \right) \right\rangle \\
&= 2\left\langle \boldsymbol{\varepsilon}^{\star\,\mathrm{HS}} \right\rangle \cdot \bar{\boldsymbol{\sigma}} - \left\langle \boldsymbol{\varepsilon}^{\star\,\mathrm{HS}} \cdot \boldsymbol{\sigma}^{\mathrm{HS}} \right\rangle + \left\langle \boldsymbol{\varepsilon}^{\star\,\mathrm{HS}} \cdot \left(\boldsymbol{p}^{\mathrm{HS}} - \mathbb{C}_0\mathbb{G}_0 * \boldsymbol{p}^{\mathrm{HS}} \right) \right\rangle \qquad (48) \\
&= 2\left\langle \boldsymbol{\varepsilon}^{\star\,\mathrm{HS}} \right\rangle \cdot \bar{\boldsymbol{\sigma}} - \left\langle \boldsymbol{\varepsilon}^{\star\,\mathrm{HS}} \cdot \boldsymbol{\sigma}^{\mathrm{HS}} \right\rangle + \left\langle \boldsymbol{\varepsilon}^{\star\,\mathrm{HS}} \cdot \left(\boldsymbol{p}^{\mathrm{HS}} - \mathbb{C}_0[\bar{\boldsymbol{\varepsilon}} - \boldsymbol{\varepsilon}^{\mathrm{HS}}] \right) \right\rangle \\
&= 2\left\langle \boldsymbol{\varepsilon}^{\star\,\mathrm{HS}} \right\rangle \cdot \bar{\boldsymbol{\sigma}} - \left\langle \boldsymbol{\varepsilon}^{\star\,\mathrm{HS}} \cdot \boldsymbol{\sigma}^{\mathrm{HS}} \right\rangle + \left\langle \boldsymbol{\varepsilon}^{\star\,\mathrm{HS}} \cdot \left(\mathbb{C}[\boldsymbol{\varepsilon}^{\mathrm{HS}}] - \bar{\boldsymbol{\sigma}} \right) \right\rangle \\
&= \left\langle \boldsymbol{\varepsilon}^{\star\,\mathrm{HS}} \right\rangle \cdot \bar{\boldsymbol{\sigma}} \\
&= \bar{\boldsymbol{\sigma}} \cdot \left(\mathbb{S}_0 - \mathbb{S}_{\boldsymbol{\sigma}}^{\mathrm{HS}} \right)[\bar{\boldsymbol{\sigma}}].
\end{aligned}
$$

References

Advani, S.G., Tucker III, C.L., 1987. The use of tensors to describe and predict fiber orientation in short fiber composites. J. Rheol. 31 (8), 751–784.

Andrä, H., Combaret, N., Dvorkin, J., Glatt, E., Han, J., Kabel, M., Keehm, Y., Krzikalla, F., Lee, M., Madonna, C., Marsh, M., Mukerji, T., Saenger, E.H., Sain, R., Saxena, N., Ricker, S., Wiegmann, A., Zhan, X., 2013a. Digital rock physics benchmarks – Part II: computing effective properties. Comput. Geosci. 50, 33–43.

Andrä, H., Grzhibovskis, R., Rjasanow, S., 2013b. Boundary element method for linear elasticity with conservative body forces. In: Apel, T., Steinbach, O. (Eds.), Advanced Finite Element Methods and Applications, Lecture Notes in Applied and Computational Mechanics, vol. 66. Springer, Berlin Heidelberg, pp. 275–297.

Bakhvalov, N., Panasenko, G., 1989. Homogenisation: Averaging Processes in Periodic Media: Mathematical Problems in the Mechanics of Composite Materials. Mathematics and its Applications. Soviet series. Kluwer Academic Publishers.

Bernasconi, A., Cosmi, F., Dreossi, D., 2008. Local anisotropy analysis of injection moulded fibre reinforced polymer composites. Compos. Sci. Technol. 68 (12), 2574–2581.

Bernasconi, A., Cosmi, F., Hine, P., 2012. Analysis of fibre orientation distribution in short fibre reinforced polymers: a comparison between optical and tomographic methods. Compos. Sci. Technol. 72 (16), 2002–2008.

Bishop, J.F.W., Hill, R., 1951a. A theoretical derivation of the plastic properties of a polycrystalline face-centred metal. Philos. Mag. 7 (42), 1298–1307.

Bishop, J.F.W., Hill, R., 1951b. A theory of the plastic distortion of a polycrystalline aggregate under combined stresses. Philos. Mag. 7 (42), 414–427.

Böhlke, T., Brüggemann, C., 2001. Graphical representation of the generalized Hooke's law. Tech. Mech. 21 (2), 145–158.

Böhlke, T., Lobos, M., 2014. Representation of Hashin–Shtrikman bounds of cubic crystal aggregates in terms of texture coefficients with application in materials design. Acta Mater.

Brisard, S., Dormieux, L., 2010. FFT-based methods for the mechanics of composites: a general variational framework. Comput. Mater. Sci. 49 (3), 663–671.

Budiansky, B., 1965. On the elastic moduli of some heterogeneous materials. J. Mech. Phys. Solids 13 (4), 223–227.

Christensen, R.M., Lo, K.H., 1979. Solutions for effective shear properties in three phase sphere and cylinder models. J. Mech. Phys. Solids 27 (4), 315–330.

Cioranescu, D., Donato, P., 1999. An Introduction to Homogenization. Oxford Lecture Series in Mathematics and Its Applications. Oxford University Press.

Dirrenberger, J., Forest, S., Jeulin, D., 2014. Towards gigantic RVE sizes for 3d stochastic fibrous networks. Int. J. Solids Struct. 51 (2), 359–376.

Doghri, I., Friebel, C., 2005. Effective elasto-plastic properties of inclusion-reinforced composites. Study of shape, orientation and cyclic response. Mech. Mater. 37 (1), 45–68.

Doghri, I., Tinel, L., 2006. Micromechanics of inelastic composites with misaligned inclusions: numerical treatment of orientation. Comput. Methods Appl. Mech. Eng. 195 (13–16), 1387–1406.

Du, D.-X., Zheng, Q.-S., 2002. A further exploration of the interaction direct derivative (IDD) estimate for the effective properties of multiphase composites taking into account inclusion distribution. Acta Mech. 157 (1–4), 61–80.

Eshelby, J.D., 1957. The determination of the elastic field of an ellipsoidal inclusion, and related problems. Proc. R. Soc. London Ser. A. Math. Phys. Sci. 241 (1226), 376–396.

Eyre, D.J., Milton, G.W., 1999. A fast numerical scheme for computing the response of composites using grid refinement. Eur. Phys. J. Appl. Phys. 6 (01), 41–47.

Frigo, M., Johnson, S., 1998. FFTW: An adaptive software architecture for the FFT. In: Acoustics, Speech and Signal Processing, 1998. Proceedings of the 1998 IEEE International Conference on Acoustics, Speech, and Signal Processing, vol. 3, pp. 1381–1384.

Frigo, M., Johnson, S., 2005. The design and implementation of FFTW3. Proc. IEEE 93 (2), 216–231.

Geers, M.G.D., Kouznetsova, V.G., Brekelmans, W.A.M., 2010. Multi-scale computational homogenization: trends and challenges. J. Comput. Appl. Math. 234 (7), 2175–2182.

GeoDict, 2014. <www.geodict.de>.

Ghosh, S., Lee, K., Moorthy, S., 1995. Multiple scale analysis of heterogeneous elastic structures using homogenization theory and Voronoi cell finite element method. Int. J. Solids Struct. 32 (1), 27–62.

Ghossein, E., Lévesque, M., 2012. A fully automated numerical tool for a comprehensive validation of homogenization models and its application to spherical particles reinforced composites. Int. J. Solids Struct. 49 (11–12), 1387–1398.

Guedes, J., Kikuchi, N., 1990. Preprocessing and postprocessing for materials based on the homogenization method with adaptive finite element methods. Comput. Methods Appl. Mech. Eng. 83 (2), 143–198.

Hashin, Z., Shtrikman, S., 1962a. On some variational principles in anisotropic and nonhomogeneous elasticity. J. Mech. Phys. Solids 10 (4), 335–342.

Hashin, Z., Shtrikman, S., 1962b. A variational approach to the theory of the elastic behaviour of polycrystals. J. Mech. Phys. Solids 10 (4), 343–352.

Hashin, Z., Shtrikman, S., 1963. A variational approach to the theory of the elastic behaviour of multiphase materials. J. Mech. Phys. Solids 11 (2), 127–140.

Hill, R., 1963. New derivations of some elastic extremum principles. Progress in Applied Mechanics: The Prager Anniversary Volume. Macmillan, New York, pp. 99–106.

Hill, R., 1965. A self-consistent mechanics of composite materials. J. Mech. Phys. Solids 13 (4), 213–222.

Johnson, S., Frigo, M., 2007. A modified split-radix FFT with fewer arithmetic operations. IEEE Trans. Signal Process. 55 (1), 111–119.

Joshi, M., Maiti, S.N., Misra, A., Mittal, R.K., 1994. Influence of fiber length, fiber orientation, and interfacial adhesion on poly (butylene terephthalate)/polyethylene alloys reinforced with short glass fibers. Polym. Compos. 15 (5), 349–358.

Kabel, M., Andrä, H., 2013. Fast numerical computation of precise bounds of effective elastic moduli. Report of the Fraunhofer ITWM 224.

Kanatani, K.-I., 1984. Distribution of directional data and fabric tensors. Int. J. Eng. Sci. 22 (2), 149–164.

Kanouté, P., Boso, D.P., Chaboche, J.L., Schrefler, B.A., 2009. Multiscale methods for composites: a review. Arch. Comput. Methods Eng. 16 (1), 31–75.

Kröner, E., 1971. Statistical Continuum Mechanics. Springer-Verlag, Wien.

Kröner, E., 1977. Bounds for effective elastic moduli of disordered materials. J. Mech. Phys. Solids 25, 137–155.

Maire, E., Withers, P.J., 2013. Quantitative x-ray tomography. Int. Mater. Rev. 59 (1), 1–43.

Michel, J.C., Moulinec, H., Suquet, P., 2001. A computational scheme for linear and non-linear composites with arbitrary phase contrast. Int. J. Numer. Methods Eng. 52 (12), 139–160.

Mori, T., Tanaka, K., 1973. Average stress in matrix and average elastic energy of materials with misfitting inclusions. Acta Metall. 21 (5), 571–574.

Moulinec, H., Suquet, P., 1994. A fast numerical method for computing the linear and nonlinear mechanical properties of composites. Comptes rendus de l'Académie des sciences. Série II, Mécanique, physique, chimie, astronomie 318 (11), 1417–1423.

Müller, V., Brylka, B., Dillenberger, F., Glöckner, R., Böhlke, T., Kolling, S., 2015. Homogenization of elastic properties of short-fiber reinforced composites based on measured microstructure data. J. Compos. Mater., in press.

Mura, T., 1987. Micromechanics of Defects in Solids,, .. Mechanics of Elastic and Inelastic Solids, revised ed. Springer.

Pierard, O., Friebel, C., Doghri, I., 2004. Mean-field homogenization of multi-phase thermo-elastic composites: a general framework and its validation. Compos. Sci. Technol. 64 (10–11), 1587–1603.

Ponte Castañeda, P., Willis, J.R., 1995. The effect of spatial distribution on the effective behavior of composite materials and cracked media. J. Mech. Phys. Solids 43 (12), 1919–1951.

Reuss, A., 1929. Berechnung der Fliegrenze von Mischkristallen auf Grund der Plastizitätsbedingung für Einkristalle. ZAMM – J. Appl. Math. Mech./Z. Angew. Math. Mech. 9 (1), 49–58.

Schladitz, K., Peters, S., Reinel-Bitzer, D., Wiegmann, A., Ohser, J., 2006. Design of acoustic trim based on geometric modeling and flow simulation for non-woven. Comput. Mater. Sci. 38 (1), 56–66.

Shen, H., Nutt, S., Hull, D., 2004. Direct observation and measurement of fiber architecture in short fiber-polymer composite foam through micro-CT imaging. Compos. Sci. Technol. 64 (13–14), 2113–2120.

Šilhavý, M., 1997. The mechanics and thermodynamics of continuous media. Texts and Monographs in Physics. Springer, New York.

Spahn, J., Andrä, H., Kabel, M., Müller, R., Linder, C. 2014. Multiscale modelling of progressive damage in elasto-plastic composite materials. In: Proceedings 11th World Congress on Computational Mechanics, Barcelona, Spain.

Suquet, P., 1987. Elements of Homogenization for Inelastic Solid Mechanics. In: Sanchez-Palencia, E., Zaoui, A. (Eds.), Homogenization Techniques in Composite Media. Springer-Verlag, Berlin, pp. 194–278.

Suquet, P.M., 1993. Overall potentials and extremal surfaces of power law or ideally plastic composites. J. Mech. Phys. Solids 41 (6), 981–1002.

Talbot, D.R.S., Willis, J.R., 1992. Some simple explicit bounds for the overall behaviour of nonlinear composites. Int. J. Solids Struct. 29 (14–15), 1981–1987.

Tomasetti, E., Legras, R., Nysten, B., 1998. Quantitative approach towards the measurement of polypropylene/(ethylene-propylene) copolymer blends surface elastic properties by AFM. Nanotechnology 9 (4), 305.

Truesdell, C., Noll, W., Jan. 2004. The non-linear field theories of mechanics. In: Antman, P.S.S. (Ed.), The Non-Linear Field Theories of Mechanics. Encyclopedia of Physics. Springer, Berlin Heidelberg, pp. 1–579.

Please cite this article in press as: Müller, V., et al. Homogenization of linear elastic properties of short-fiber reinforced composites – A comparison of mean field and voxel-based methods. Int. J. Solids Struct. (2015), http://dx.doi.org/10.1016/j.ijsolstr.2015.02.030

Voigt, W., 1889. Über die Beziehung zwischen den beiden Elastizitätskonstanten isotroper Körper. Ann. Phys. 274 (12), 573–587.
Willis, J.R., 1977. Bounds and self-consistent estimates for the overall properties of anisotropic composites. J. Mech. Phys. Solids 25 (3), 185–202.
Willis, J.R., 1978. Variational principles and bounds for the overall properties of composites. Contin. Models Discrete Syst., 185–215
Willis, J.R., 1981. Variational and related methods for the overall properties of composites. Advances in Applied Mechanics, vol. 21. Elsevier, pp. 1–78.
Willis, J.R., 1986. Variational estimates for the overall response of an inhomogeneous nonlinear dielectric. In: Ericksen, J.L., Kinderlehrer, D., Kohn, R., Lions, J.-L. (Eds.), Homogenization and Effective Moduli of Materials and Media, No. 1 in The IMA Volumes in Mathematics and its Applications. Springer, New York, pp. 247–263.
Zeller, R., Dederichs, P.H., 1973. Elastic constants of polycrystals. Phys. Status Solidi (B) 55 (2), 831–842.
Zheng, Q.S., Du, D.X., 2001. An explicit and universally applicable estimate for the effective properties of multiphase composites which accounts for inclusion distribution. J. Mech. Phys. Solids 49 (11), 2765–2788.

Please cite this article in press as: Müller, V., et al. Homogenization of linear elastic properties of short-fiber reinforced composites – A comparison of mean field and voxel-based methods. Int. J. Solids Struct. (2015), http://dx.doi.org/10.1016/j.ijsolstr.2015.02.030